

ALICE-ANA-2016-xxx  
June 14, 2017

## Lambda-Kaon and Cascade-Kaon Femtoscopy in Pb-Pb Collisions at $\sqrt{s_{NN}} = 2.76 \text{ TeV}$ from the LHC ALICE Experiment

Jesse T. Buxton<sup>1</sup>

1. Department of Physics, The Ohio State University, Columbus, Ohio, USA

Email: jesse.thomas.buxton@cern.ch

### Abstract

We present results from a femtoscopic analysis of Lambda-Kaon correlations in Pb-Pb collisions at  $\sqrt{s_{NN}} = 2.76 \text{ TeV}$  by the ALICE experiment at the LHC. All pair combinations of  $\Lambda$  and  $\bar{\Lambda}$  with  $K^+$ ,  $K^-$  and  $K_S^0$  are analyzed. The femtoscopic correlations are the result of strong final-state interactions, and are fit with a parametrization based on a model by R. Lednicky and V. L. Lyuboshitz [1]. This allows us to both characterize the emission source and measure the scattering parameters for the particle pairs. We observe a large difference in the  $\Lambda$ - $K^+$  ( $\bar{\Lambda}$ - $K^-$ ) and  $\Lambda$ - $K^-$  ( $\bar{\Lambda}$ - $K^+$ ) correlations in pairs with low relative momenta ( $k^* \lesssim 100 \text{ MeV}$ ). Additionally, the average of the  $\Lambda$ - $K^+$  ( $\bar{\Lambda}$ - $K^-$ ) and  $\Lambda$ - $K^-$  ( $\bar{\Lambda}$ - $K^+$ ) correlation functions is consistent with our  $\Lambda$ - $K_S^0$  ( $\bar{\Lambda}$ - $K_S^0$ ) measurement. The results suggest an effect arising from different quark-antiquark interactions in the pairs, i.e.  $s\bar{s}$  in  $\Lambda$ - $K^+$  ( $\bar{\Lambda}$ - $K^-$ ) and  $u\bar{u}$  in  $\Lambda$ - $K^-$  ( $\bar{\Lambda}$ - $K^+$ ). To gain further insight into this hypothesis, we currently are conducting a  $\Xi$ -K femtoscopic analysis.



## Contents

<b>1</b>	<b>Introduction</b>	<b>4</b>
<b>2</b>	<b>Data Sample and Software</b>	<b>4</b>
2.1	Data Sample . . . . .	4
2.2	Software . . . . .	4
<b>3</b>	<b>Data Selection</b>	<b>4</b>
3.1	Event Selection and Mixing . . . . .	4
3.2	K $^{\pm}$ Track Selection . . . . .	5
3.3	V0 Selection . . . . .	6
3.3.1	Λ Reconstruction . . . . .	7
3.3.2	K $_S^0$ Reconstruction . . . . .	9
3.4	Cascade Reconstruction . . . . .	10
3.5	Pair Selection . . . . .	13
<b>4</b>	<b>Correlation Functions</b>	<b>14</b>
<b>5</b>	<b>Fitting</b>	<b>15</b>
5.1	Model: ΛK $_S^0$ , ΛK $^{\pm}$ , Ξ $^{ch}$ K $_S^0$ . . . . .	15
5.2	Model: Ξ $^{ch}$ K $^{ch}$ . . . . .	18
5.3	Momentum Resolution Corrections . . . . .	21
5.4	Residual Correlations . . . . .	23
<b>6</b>	<b>Systematic Errors</b>	<b>24</b>
6.1	Systematic Errors: ΛK $_S^0$ . . . . .	26
6.1.1	Particle and Pair Cuts . . . . .	26
6.1.2	Non-Flat Background . . . . .	27
6.1.3	Fit Range . . . . .	27
6.2	Systematic Errors: ΛK $^{\pm}$ . . . . .	27
6.2.1	Particle and Pair Cuts . . . . .	27
6.2.2	Non-Flat Background . . . . .	28
6.2.3	Fit Range . . . . .	28
6.3	Systematic Errors: ΞK $^{\pm}$ . . . . .	28
6.3.1	Particle and Pair Cuts . . . . .	28

<b>7 Results and Discussion</b>	<b>29</b>
7.1 Results: $\Lambda K_S^0$ and $\Lambda K^\pm$ . . . . .	29
7.2 Results: $\Xi K^\pm$ . . . . .	38
<b>8 To Do</b>	<b>40</b>

## List of Figures

1	V0 Reconstruction	7
2	$K_S^0$ contamination in $\Lambda(\bar{\Lambda})$ collection	8
3	$\Lambda$ and $\bar{\Lambda}$ Purity	9
4	$\Lambda(\bar{\Lambda})$ contamination in $K_S^0$ collection	11
5	$K_S^0$ Purity	12
6	$\Xi$ Reconstruction	13
7	$\Xi^-(\bar{\Xi}^+)$ Purity	13
8	Average Separation of $\Lambda(\bar{\Lambda})$ and $K_S^0$ Daughters	15
9	Average Separation of $\Lambda(\bar{\Lambda})$ Daughter and $K^\pm$	16
10	Average Separation of $\Xi$ Daughters and $K^\pm$	17
11	$\Lambda(\bar{\Lambda})K_S^0$ Correlation Functions	18
12	$\Lambda K^+$ and $\bar{\Lambda} K^-$ Correlation Functions	19
13	$\Lambda K^-$ and $\bar{\Lambda} K^+$ Correlation Functions	20
14	Correlation Functions: $\Lambda K^+$ vs $\Lambda K^-$ for 0-10% Centrality	21
15	Momentum Resolution: Sample $k_{True}^*$ vs. $k_{Rec}^*$	24
16	Particle Contaminations Visible in $k_{True}^*$ vs. $k_{Rec}^*$	25
17	Transform Matrices for $\Lambda K^+$ Analysis	26
18	Transform Matrices for $\bar{\Lambda} K^+$ Analysis	27
19	$\Lambda K_S^0(\bar{\Lambda} K_S^0)$ Fits	30
20	$\Lambda K_S^0(\bar{\Lambda} K_S^0)$ Fits (Wide Range)	31
21	$\Lambda K^+(\bar{\Lambda} K^-)$ Fits	32
22	$\Lambda K^+(\bar{\Lambda} K^-)$ Fits (Wide Range)	33
23	$\Lambda K^-(\bar{\Lambda} K^+)$ Fits	34
24	$\Lambda K^-(\bar{\Lambda} K^+)$ Fits (Wide Range)	35
25	$m_T$ Scaling of Radii	38
26	$\Xi K^\pm$ Results	38
27	$\Xi K^\pm$ Data with Coulomb-Only Bands, 0-10% Centrality	39
28	Effect of Strong Force Inclusion on Coulomb-Only Curve for $\Xi K^\pm$ systems	41
29	$\Xi K^\pm$ Global Coulomb-Only Fit (Set 1)	42
30	$\Xi K^\pm$ Global Coulomb-Only Fit (Set 2)	43
31	$\Xi^- K^+$ Coulomb-Only Fit	43
32	$\Xi^- K^-$ Coulomb-Only Fit	44

---

## 12 1 Introduction

13 We present results from a femtoscopic analysis of Lambda-Kaon correlations in Pb-Pb collisions at  $\sqrt{s_{NN}}$   
 14 = 2.76 TeV by the ALICE experiment at the LHC. All pair combinations of  $\Lambda$  and  $\bar{\Lambda}$  with  $K^+$ ,  $K^-$  and  
 15  $K_S^0$  are analyzed. The femtoscopic correlations are the result of strong final-state interactions, and are  
 16 fit with a parametrization based on a model by R. Lednicky and V. L. Lyuboshitz [1]. This allows us to  
 17 both characterize the emission source and measure the scattering parameters for the particle pairs. We  
 18 observe a large difference in the  $\Lambda$ - $K^+$  ( $\bar{\Lambda}$ - $K^-$ ) and  $\Lambda$ - $K^-$  ( $\bar{\Lambda}$ - $K^+$ ) correlations in pairs with low relative  
 19 momenta ( $k^* \lesssim 100$  MeV). Additionally, the average of the  $\Lambda$ - $K^+$  ( $\bar{\Lambda}$ - $K^-$ ) and  $\Lambda$ - $K^-$  ( $\bar{\Lambda}$ - $K^+$ ) correlation  
 20 functions is consistent with our  $\Lambda$ - $K_S^0$  ( $\bar{\Lambda}$ - $K_S^0$ ) measurement. The results suggest an effect arising from  
 21 different quark-antiquark interactions in the pairs, i.e.  $s\bar{s}$  in  $\Lambda$ - $K^+$  ( $\bar{\Lambda}$ - $K^-$ ) and  $u\bar{u}$  in  $\Lambda$ - $K^-$  ( $\bar{\Lambda}$ - $K^+$ ). To  
 22 gain further insight into this hypothesis, we currently are conducting a  $\Xi$ -K femtoscopic analysis.

## 23 2 Data Sample and Software

### 24 2.1 Data Sample

25 The analysis used “pass 2” reconstructed Pb-Pb data from LHC11h (AOD145). The runlist was selected  
 26 from runs with global quality tag “1” in the ALICE Run Condition Table. Approximately 40 million  
 27 combined central, semi-central, and minimum bias events were analyzed. Runs from both positive (++)  
 28 and negative (--) magnetic field polarity settings were used.

29 Run list: 170593, 170572, 170388, 170387, 170315, 170313, 170312, 170311, 170309, 170308, 170306,  
 30 170270, 170269, 170268, 170230, 170228, 170207, 170204, 170203, 170193, 170163, 170159, 170155,  
 31 170091, 170089, 170088, 170085, 170084, 170083, 170081, 170040, 170027, 169965, 169923, 169859,  
 32 169858, 169855, 169846, 169838, 169837, 169835, 169591, 169590, 169588, 169587, 169586, 169557,  
 33 169555, 169554, 169553, 169550, 169515, 169512, 169506, 169504, 169498, 169475, 169420, 169419,  
 34 169418, 169417, 169415, 169411, 169238, 169167, 169160, 169156, 169148, 169145, 169144, 169138,  
 35 169099, 169094, 169091, 169045, 169044, 169040, 169035, 168992, 168988, 168826, 168777, 168514,  
 36 168512, 168511, 168467, 168464, 168460, 168458, 168362, 168361, 168342, 168341, 168325, 168322,  
 37 168311, 168310, 168315, 168108, 168107, 168105, 168076, 168069, 167988, 167987, 167985, 167920,  
 38 167915

39 Analysis was also performed on the LHC12a17a\_fix (AOD149) Monte Carlo HIJING events for certain  
 40 checks. THERMINATOR2 was also used for certain aspects, such as transform matrices described feed-  
 41 down contributions.

### 42 2.2 Software

43 The analysis was performed on the PWGCF analysis train using AliRoot v5-08-18-1 and AliPhysics  
 44 vAN-20161027-1.

45 The main classes utilized include: AliFemtoVertexMultAnalysis, AliFemtoEventCutEstimators, AliFem-  
 46 toESDTrackCutNSigmaFilter, AliFemtoV0TrackCutNSigmaFilter, AliFemtoXiTrackCut, AliFemtoV0PairCut,  
 47 AliFemtoV0TrackPairCut, AliFemtoXiTrackPairCut, and AliFemtoAnalysisLambdaKaon. All of these  
 48 classes are contained in /AliPhysics/PWGCF/FEMTOSCOPY/AliFemto and .../AliFemtoUser.

## 49 3 Data Selection

### 50 3.1 Event Selection and Mixing

51 The events used in this study were selected with the class AliFemtoEventCutEstimators according to the  
 52 following criteria:

- 53        – Triggers
- 54            – minimum bias (kMB)
- 55            – central (kCentral)
- 56            – semi-central (kSemiCentral)
- 57        – z-position of reconstructed event vertex must be within 10 cm of the center of the ALICE detector
- 58        – the event must contain at least one particle of each type from the pair of interest

59     The event mixing was handled by the AliFemtoVertexMultAnalysis class, which only mixes events with  
60     like vertex position and centrality. The following criteria were used for event mixing:

- 61        – Number of events to mix = 5
- 62        – Vertex position bin width = 2 cm
- 63        – Centrality bin width = 5

64     The AliFemtoEventReaderAODChain class is used to read the events. Event flattening is not currently  
65     used. FilterBit(7). The centrality is determined by the “V0M” method of AliCentrality, set by calling Al-  
66     iFemtoEventReaderAOD::SetUseMultiplicity(kCentrality). I utilize the SetPrimaryVertexCorrectionT-  
67     PCPoints switch, which causes the reader to shift all TPC points to be relative to the event vertex.

### 68     3.2 K $^{\pm}$ Track Selection

69     Charged kaons are identified using the AliFemtoESDTrackCutNSigmaFilter class. The specific cuts used  
70     in this analysis are as follows:

71     Track Selection:

- 72        – Kinematic range:
- 73            –  $0.14 < p_T < 1.5$
- 74            –  $|\eta| < 0.8$
- 75        – FilterBit(7)
- 76            – TPC tracks
- 77        – Track Quality
- 78            – Minimum number of clusters in the TPC (fminTPCncls) = 80
- 79            – Maximum allowed  $\chi^2/N_{DOF}$  for ITS clusters = 3.0
- 80            – Maximum allowed  $\chi^2/N_{DOF}$  for TPC clusters = 4.0
- 81        – Primary Particle Selection:
- 82            – Maximum XY impact parameter = 2.4
- 83            – Maximum Z impact parameter = 3.0
- 84        – Remove particles with any kink labels (fRemoveKinks = true)
- 85        – Maximum allowed sigma to primary vertex (fMaxSigmaToVertex) = 3.0

86 K $^\pm$  Identification:

87 – PID Probabilities:

- 88 – K: > 0.2
- 89 –  $\pi$ : < 0.1
- 90 –  $\mu$ : < 0.8
- 91 – p: < 0.1

92 – Most probable particle type must be Kaon (fMostProbable=3)

93 – TPC and TOF N $_\sigma$  cuts:

- 94 –  $p < 0.4 \text{ GeV}/c$ :  $N_{\sigma K, TPC} < 2$
- 95 –  $0.4 < p < 0.45 \text{ GeV}/c$ :  $N_{\sigma K, TPC} < 1$
- 96 –  $0.45 < p < 0.8 \text{ GeV}/c$ :  $N_{\sigma K, TPC} < 3 \& N_{\sigma K, TOF} < 2$
- 97 –  $0.8 < p < 1.0 \text{ GeV}/c$ :  $N_{\sigma K, TPC} < 3 \& N_{\sigma K, TOF} < 1.5$
- 98 –  $p > 1.0 \text{ GeV}/c$ :  $N_{\sigma K, TPC} < 3 \& N_{\sigma K, TOF} < 1$

99 – Electron Rejection: Reject if  $N_{\sigma e^-, TPC} < 3$

100 – Pion Rejection: Reject if:

- 101 –  $p < 0.65$ 
  - 102 \* if TOF and TPC available:  $N_{\sigma \pi, TPC} < 3 \& N_{\sigma \pi, TOF} < 3$
  - 103 \* else
    - 104 ·  $p < 0.5$ :  $N_{\sigma \pi, TPC} < 3$
    - 105 ·  $0.5 < p < 0.65$ :  $N_{\sigma \pi, TPC} < 2$
- 106 –  $0.65 < p < 1.5$ :  $N_{\sigma \pi, TPC} < 5 \& N_{\sigma \pi, TOF} < 3$
- 107 –  $p > 1.5$ :  $N_{\sigma \pi, TPC} < 5 \& N_{\sigma \pi, TOF} < 2$

108 The purity of the K $^\pm$  collections was estimated using the MC data, for which the true identity of each  
109 reconstructed K $^\pm$  particle is known. Therefore, the purity may be estimated as:

$$\text{Purity}(K^\pm) = \frac{N_{true}}{N_{reconstructed}} \quad (1)$$

110 Purity(K $^+$ )  $\approx$  Purity(K $^-$ )  $\approx$  97%

### 111 3.3 V0 Selection

112  $\Lambda$  ( $\bar{\Lambda}$ ) and K $_S^0$  are neutral particles which cannot be directly detected, but must instead be reconstructed  
113 through detection of their decay products, or daughters. This process is illustrated in Figure 1. In  
114 general, particles which are topologically reconstructed in this fashion are called V0 particles. The  
115 class AliFemtoV0TrackCutNSigmaFilter (which is an extension of AliFemtoV0TrackCut) is used to  
116 reconstruct the V0s.

117 In order to obtain a true and reliable signal, one must ensure good purity of the V0 collection. The purity  
118 of the collection is calculated as:

$$\text{Purity}_y = \frac{\text{Signal}}{\text{Signal} + \text{Background}} \quad (2)$$

119 To obtain both the signal and background, the invariant mass distribution ( $m_{inv}$ ) of all V0 candidates  
 120 must be constructed immediately before the final invariant mass cut. Examples of such distributions can  
 121 be found in Figures 3 and 5. It is vital that this distribution be constructed immediately before the final  
 122  $m_{inv}$  cut, otherwise it would be impossible to estimate the background. As shown in Figures 3 and 5, the  
 123 background is fit (with a polynomial) outside of the peak region of interest to obtain an estimate for the  
 124 background within the region. Within the  $m_{inv}$  cut limits, the background is the region below the fit while  
 125 the signal is the region above the fit.

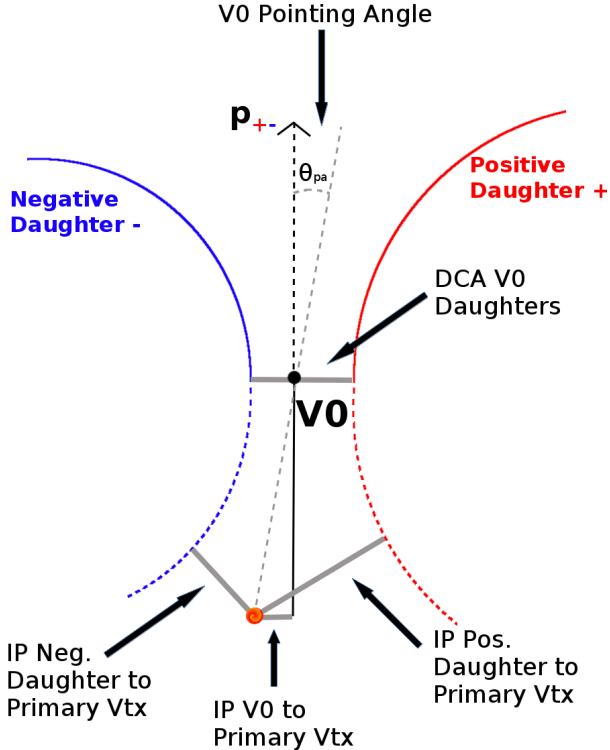


**Fig. 1:** V0 Reconstruction

### 126 3.3.1 $\Lambda$ Reconstruction

127 The following cuts were used to select good  $\Lambda$  ( $\bar{\Lambda}$ ) candidates:

128 1. Daughter Particle Cuts

- 129 (a) Cuts Common to Both Daughters
- 130     i.  $|\eta| < 0.8$
- 131     ii. SetTPCnclsDaughters(80)
- 132     iii. SetStatusDaughters(AliESDtrack::kTPCrefic)
- 133     iv. SetMaxDcaV0Daughters(0.4)

134 (b) Pion Specific Daughter Cuts

- 135     i.  $p_T > 0.16$
- 136     ii. DCA to prim vertex  $> 0.3$

137 (c) Proton Specific Daughter Cuts

- 138     i.  $p_T > 0.5(p) [0.3(\bar{p})] \text{ GeV}/c$
- 139     ii. DCA to prim vertex  $> 0.1$

140    2. V0 Cuts

- 141    (a)  $|\eta| < 0.8$   
 142    (b)  $p_T > 0.4$   
 143    (c)  $|m_{inv} - m_{PDG}| < 3.8 \text{ MeV}$   
 144    (d) DCA to prim. vertex  $< 0.5 \text{ cm}$   
 145    (e) Cosine of pointing angle  $> 0.9993$   
 146    (f) OnFlyStatus = false  
 147    (g) Decay Length  $< 60 \text{ cm}$

148    3. Shared Daughter Cut for V0 Collection

- 149    – Iterate through V0 collection to ensure that no daughter is used in more than one V0 candidate

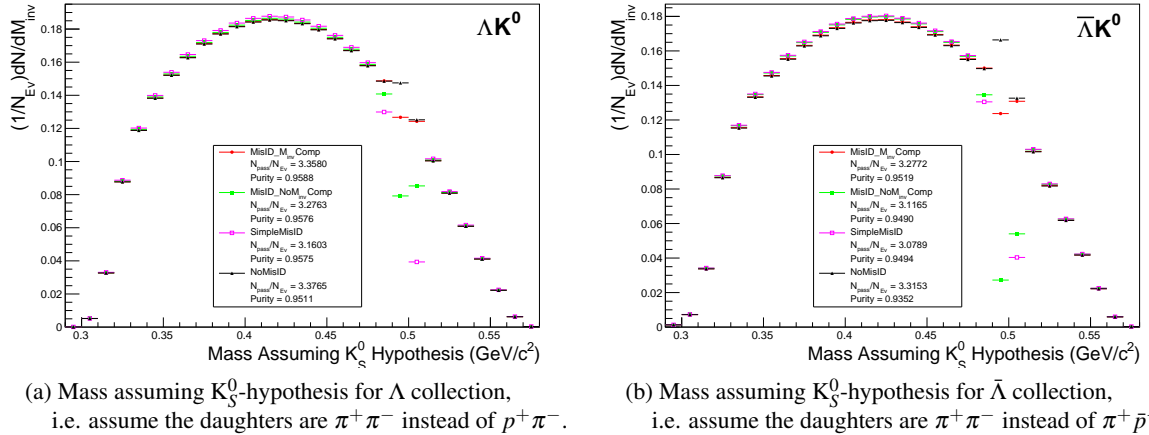


**Fig. 2:** Mass assuming  $K_S^0$ -hypothesis for V0 candidates passing all  $\Lambda$  (2a) and  $\bar{\Lambda}$  (2b) cuts. The “NoMisID” distribution (black triangles) uses the V0 finder without any attempt to remove misidentified  $K_S^0$ . The slight peak in the “NoMisID” distribution around  $m_{inv} = 0.5 \text{ GeV}/c^2$  contains misidentified  $K_S^0$  particles in our  $\Lambda(\bar{\Lambda})$  collection. “SimpleMisID” (pink squares) simply cuts out the entire peak, which throws away some good  $\Lambda$  and  $\bar{\Lambda}$  particles. “MisID\_NoM<sub>inv</sub>\_Comp” (green squares) uses the misidentification cut outlined in the text, but does not utilize the invariant mass comparison method. “MisID\_M<sub>inv</sub>\_Comp” (red circles) utilizes the full misidentification methods, and is currently used for this analysis. “ $N_{pass}/N_{ev}$ ” is the total number of  $\Lambda(\bar{\Lambda})$  particles found, normalized by the total number of events. The purity of the collection is also listed.

150    Figure 2a shows the mass assuming  $K_S^0$  hypothesis for the  $\Lambda$  collection, i.e. assume the daughters are  
 151     $\pi^+\pi^-$  instead of  $\pi^+\bar{p}^-$ . Figure 2b is a similar plot, but is for the  $\bar{\Lambda}$  collection, i.e. assume the daughters  
 152    are  $\pi^+\pi^-$  instead of  $\pi^+\bar{p}^-$ . The  $K_S^0$  contamination is visible, although not profound, in both in the slight  
 153    peaks around  $m_{inv} = 0.497 \text{ GeV}/c^2$ . If one simply cuts out the entire peak, good  $\Lambda$  particles will be  
 154    lost. Ideally, the  $\Lambda$  selection and  $K_S^0$  misidentification cuts are selected such that the peak is removed  
 155    from this plot while leaving the distribution continuous. To attempt to remove these  $K_S^0$  contaminations  
 156    without throwing away good  $\Lambda$  and  $\bar{\Lambda}$  particles, the following misidentification cuts are imposed; a  $\Lambda(\bar{\Lambda})$   
 157    candidate is rejected if all of the following criteria are satisfied:

- 158    –  $|m_{inv, K_S^0 \text{ Hypothesis}} - m_{PDG, K_S^0}| < 9.0 \text{ MeV}/c^2$   
 159    – Positive and negative daughters pass  $\pi$  daughter cut implemented for  $K_S^0$  reconstruction

$$160 \quad - \left| m_{inv, K_S^0 \text{ Hypothesis}} - m_{PDG, K_S^0} \right| < \left| m_{inv, \Lambda(\bar{\Lambda}) \text{ Hypothesis}} - m_{PDG, \Lambda(\bar{\Lambda})} \right|$$

161 Figure 3 shows the invariant mass ( $M_{inv}$ ) distribution of all  $\Lambda(\bar{\Lambda})$  candidates immediately before the final  
 162 invariant mass cut. These distributions are used to calculate the collection purities. The  $\Lambda$  and  $\bar{\Lambda}$  purities  
 163 are found to be: Purity( $\Lambda$ )  $\approx$  Purity( $\bar{\Lambda}$ )  $\approx$  95%.

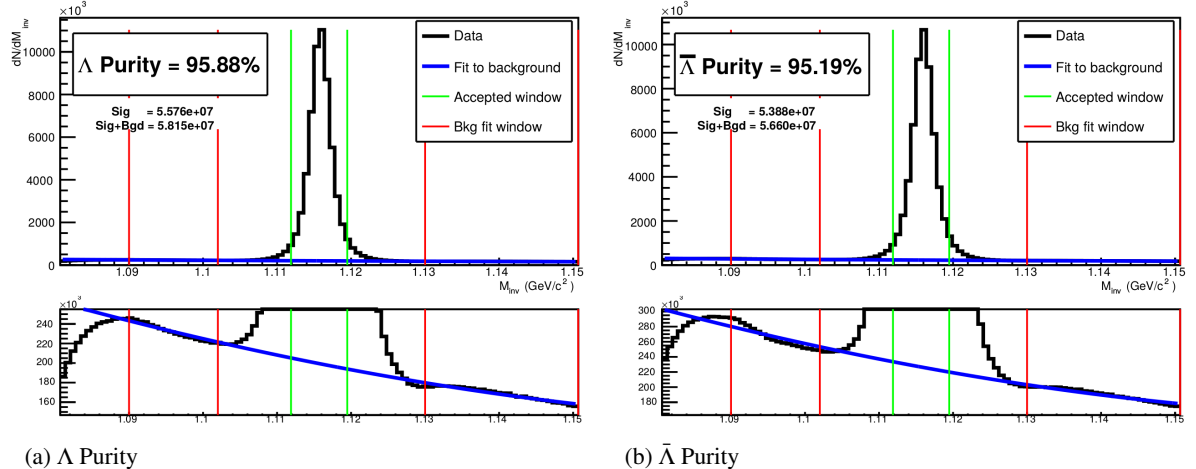


**Fig. 3:** Invariant mass ( $M_{inv}$ ) distribution of all  $\Lambda$  (a) and  $\bar{\Lambda}$  (b) candidates immediately before the final invariant mass cut. The bottom figures are zoomed to show the background with fit. The vertical green lines represent the  $M_{inv}$  cuts used in the analyses, the red vertical lines delineate the region over which the background was fit, and the blue line shows the background fit. These distributions are used to calculate the collection purities, Purity( $\Lambda$ )  $\approx$  Purity( $\bar{\Lambda}$ )  $\approx$  95%.

### 164 3.3.2 $K_S^0$ Reconstruction

165 The following cuts were used to select good  $K_S^0$  candidates:

166 1. Pion Daughter Cuts

- 167 (a)  $|\eta| < 0.8$
- 168 (b) SetTPCnclsDaughters(80)
- 169 (c) SetStatusDaughters(AliESDtrack::kTPCrefic)
- 170 (d) SetMaxDcaV0Daughters(0.3)
- 171 (e)  $p_T > 0.15$
- 172 (f) DCA to prim vertex  $> 0.3$

173 2.  $K_S^0$  Cuts

- 174 (a)  $|\eta| < 0.8$
- 175 (b)  $p_T > 0.2$
- 176 (c)  $m_{PDG} - 13.677 \text{ MeV} < m_{inv} < m_{PDG} + 2.0323 \text{ MeV}$
- 177 (d) DCA to prim. vertex  $< 0.3 \text{ cm}$
- 178 (e) Cosine of pointing angle  $> 0.9993$
- 179 (f) OnFlyStatus = false
- 180 (g) Decay Length  $< 30 \text{ cm}$

181     3. Shared Daughter Cut for V0 Collection

- 182       – Iterate through V0 collection to ensure that no daughter is used in more than one V0 candidate

183     As can be seen in Figure 4, some misidentified  $\Lambda$  and  $\bar{\Lambda}$  particles contaminate our  $K_S^0$  sample. Figure  
 184     4a shows the mass assuming  $\Lambda$ -hypothesis for the  $K_S^0$  collection, i.e. assume the daughters are  $p^+\pi^-$   
 185     instead of  $\pi^+\pi^-$ . Figure 4b is similar, but shows the mass assuming  $\bar{\Lambda}$  hypothesis for the collection,  
 186     i.e. assume the daughters are  $\pi^+\bar{p}^-$  instead of  $\pi^+\pi^-$ . The  $\Lambda$  contamination can be seen in 4a, and the  
 187      $\bar{\Lambda}$  contamination in 4b, in the peaks around  $m_{inv} = 1.115 \text{ GeV}/c^2$ . Additionally, the  $\bar{\Lambda}$  contamination is  
 188     visible in Figure 4a, and the  $\Lambda$  contamination visible in Figure 4b, in the region of excess around  $1.65$   
 189      $< m_{inv} < 2.1 \text{ GeV}/c^2$ . This is confirmed as the number of misidentified  $\Lambda$  particles in the sharp peak  
 190     of Figure 4a (misidentified  $\bar{\Lambda}$  particles in the sharp peak of Figure 4b) approximately equals the excess  
 191     found in the  $1.65 < m_{inv} < 2.1 \text{ GeV}/c^2$  region of Figure 4a (Figure 4b).

192     The peaks around  $m_{inv} = 1.115 \text{ GeV}/c^2$  in Figure 4 contain both misidentified  $\Lambda$  ( $\bar{\Lambda}$ ) particles and good  
 193      $K_S^0$ . If one simply cuts out the entire peak, some good  $K_S^0$  particles will be lost. Ideally, the  $K_S^0$  selection  
 194     and  $\Lambda(\bar{\Lambda})$  misidentification cuts can be selected such that the peak is removed from this plot while leaving  
 195     the distribution continuous. To attempt to remove these  $\Lambda$  and  $\bar{\Lambda}$  contaminations without throwing away  
 196     good  $K_S^0$  particles, the following misidentification cuts are imposed; a  $K_S^0$  candidate is rejected if all of  
 197     the following criteria are satisfied (for either  $\Lambda$  or  $\bar{\Lambda}$  hypothesis):

- 198       –  $|m_{inv, \Lambda(\bar{\Lambda}) \text{ Hypothesis}} - m_{PDG, \Lambda(\bar{\Lambda})}| < 9.0 \text{ MeV}/c^2$
- 199       – Positive daughter passes  $p^+(\pi^+)$  daughter cut implemented for  $\Lambda(\bar{\Lambda})$  reconstruction
- 200       – Negative daughter passes  $\pi^-(\bar{p}^-)$  daughter cut implemented by  $\Lambda(\bar{\Lambda})$  reconstruction
- 201       –  $|m_{inv, \Lambda(\bar{\Lambda}) \text{ Hypothesis}} - m_{PDG, \Lambda(\bar{\Lambda})}| < |m_{inv, K_S^0 \text{ Hypothesis}} - m_{PDG, K_S^0}|$

202     **3.4 Cascade Reconstruction**

203     Our motivation for studying  $\Xi K^\pm$  systems is to hopefully better understand the striking difference in the  
 204      $\Lambda K^+$  and  $\Lambda K^-$  data at low  $k^*$  (Figure 14).

205     The reconstruction of  $\Xi$  particles is one step above V0 reconstruction. V0 particles are topologically  
 206     reconstructed by searching for the charged daughters' tracks into which they decay. With  $\Xi$  particles, we  
 207     search for the V0 particle and charged daughter into which the  $\Xi$  decays. In the case of  $\Xi^-$ , we search  
 208     for the  $\Lambda$  (V0) and  $\pi^-$  (track) daughters. We will refer to this  $\pi$  as the “bachelor  $\pi$ ”.

209     The following cuts were used to select good  $\Xi^- (\bar{\Xi}^+)$  candidates:

210       1. V0 Daughter Reconstruction

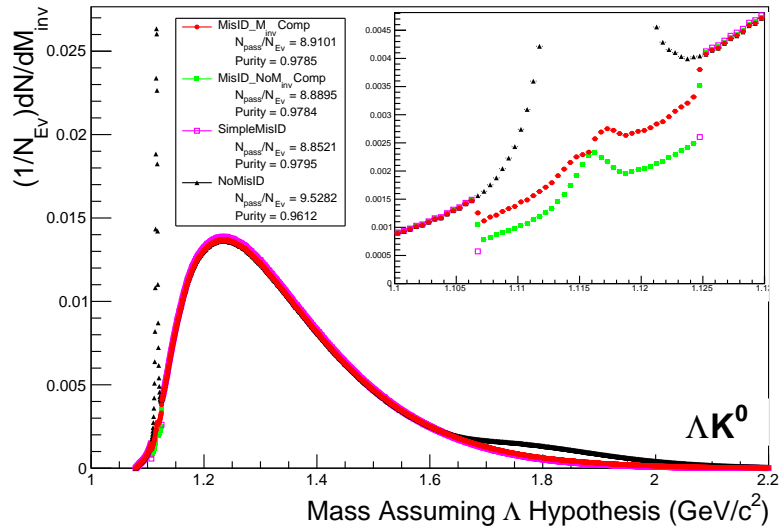
211           (a) V0 Daughter Particle Cuts

212              i. Cuts Common to Both Daughters

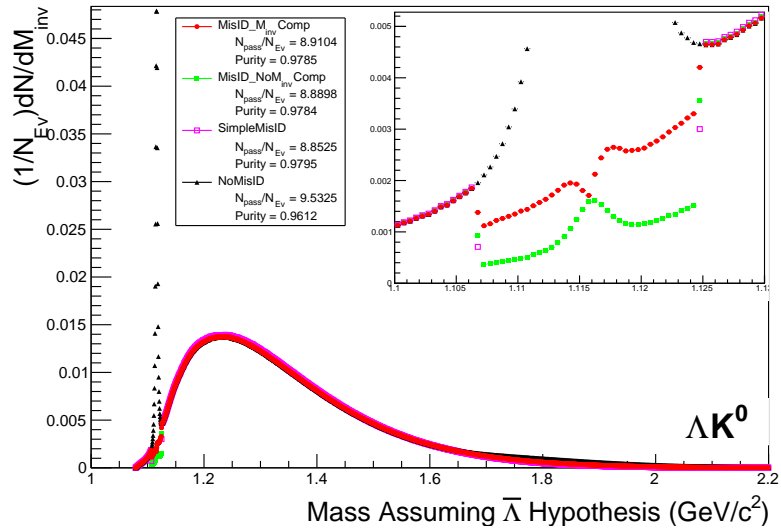
- 213               A.  $|\eta| < 0.8$
- 214               B. SetTPCnclsDaughters(80)
- 215               C. SetStatusDaughters(AliESDtrack::kTPCrefic)
- 216               D. SetMaxDcaV0Daughters(0.4)

217              ii. Pion Specific Daughter Cuts

- 218               A.  $p_T > 0.16$



(a) Mass assuming  $\Lambda$ -hypothesis for  $K_S^0$  collection, i.e. assume the daughters are  $p^+ \pi^-$  instead of  $\pi^+ \pi^-$ .



(b) Mass assuming  $\bar{\Lambda}$ -hypothesis for  $K_S^0$  collection, i.e. assume the daughters are  $p^+ \bar{p}^-$  instead of  $\pi^+ \pi^-$ .

**Fig. 4:** Mass assuming  $\Lambda$ -hypothesis (4a) and  $\bar{\Lambda}$ -hypothesis (4b) for  $K_S^0$  collection. The “NoMisID” distribution (black triangles) uses the V0 finder without any attempt to remove misidentified  $\Lambda$  and  $\bar{\Lambda}$ . The peak in the “NoMisID” distribution around  $m_{\text{inv}} = 1.115 \text{ GeV}/c^2$  contains misidentified  $\Lambda$  (4a) and  $\bar{\Lambda}$  (4b) particles in our  $K_S^0$  collection. “SimpleMisID” (pink squares) simply cuts out the entire peak, which throws away some good  $K_S^0$  particles. “MisID\_NoM<sub>inv</sub>Comp” (green squares) uses the misidentification cut outlined in the text, but does not utilize the invariant mass comparison method. “MisID\_M<sub>inv</sub>Comp” (red circles) utilizes the full misidentification methods, and is currently used for this analysis. “ $N_{\text{pass}}/N_{\text{ev}}$ ” is the total number of  $K_S^0$  particles found, normalized by the total number of events. The purity of the collection is also listed. Also note, the relative excess of the “NoMisID” distribution around  $1.65 < m_{\text{inv}} < 2.1 \text{ GeV}/c^2$  shows misidentified  $\bar{\Lambda}$  (4a) and  $\Lambda$  (4b) particles in our  $K_S^0$  collection.

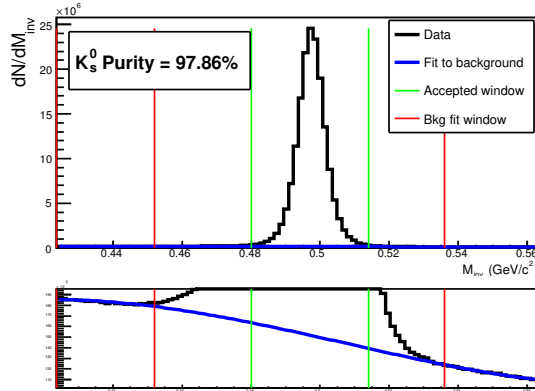


**Fig. 5:** Invariant mass ( $M_{inv}$ ) distribution of all  $K_s^0$  candidates immediately before the final invariant mass cut. The bottom figure is zoomed to show the background with fit. The vertical green lines represent the  $M_{inv}$  cut used in the analyses, the red vertical lines delineate the region over which the background was fit, and the blue line shows the background fit. This distribution is used to calculate the collection purity,  $Purity(K_s^0) \approx 98\%$ .

221                   A.  $p_T > 0.5(p)[0.3(\bar{p})] \text{ GeV}/c$

222                   B. DCA to prim vertex  $> 0.1$

223                   (b) V0 Cuts

224                   i.  $|\eta| < 0.8$

225                   ii.  $p_T > 0.4 \text{ GeV}/c$

226                   iii.  $|m_{inv} - m_{PDG}| < 3.8 \text{ MeV}$

227                   iv. DCA to prim. vertex  $> 0.2 \text{ cm}$

228                   v. Cosine of pointing angle to  $\Xi$  decay vertex  $> 0.9993$

229                   vi. OnFlyStatus = false

230                   vii. Decay Length  $< 60 \text{ cm}$

231                   viii. The misidentification cuts described in Section 3.3.1 are utilized

232                   2. Bachelor  $\pi$  Cuts

233                   (a)  $|\eta| < 0.8$

234                   (b)  $p_T < 100 \text{ GeV}/c$

235                   (c) DCA to prim vertex  $> 0.1 \text{ cm}$

236                   (d) SetTPCnclsDaughters(70)

237                   (e) SetStatusDaughters(AliESDtrack::kTPCrefic)

238                   3.  $\Xi$  Cuts

239                   (a)  $|\eta| < 0.8$

240                   (b)  $0.8 < p_T < 100 \text{ GeV}/c$

241                   (c)  $|m_{inv} - m_{PDG}| < 3.0 \text{ MeV}$

242                   (d) DCA to prim. vertex  $< 0.3 \text{ cm}$

243                   (e) Cosine of pointing angle  $> 0.9992$

244                   4. Shared Daughter Cut for  $\Xi$  Collection

- Iterate through  $\Xi$  collection to ensure that no daughter is used in more than one  $\Xi$  candidate

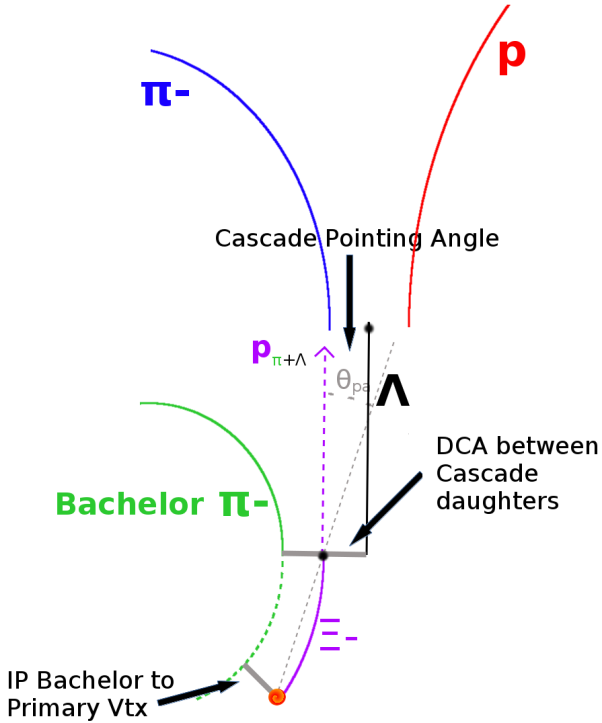


**Fig. 6:**  $\Xi$  Reconstruction

246 The purity of our  $\Xi$  and  $\bar{\Xi}$  collections are calculated just as those of our V0 collections 3.3. Figure 7,  
247 which is used to calculate the purity, shows the  $m_{inv}$  distribution of our  $\Xi(\bar{\Xi})$  candidates just before the  
248 final  $m_{inv}$  cut. Currently, we have Purity( $\Xi^-$ )  $\approx$  90% and Purity( $\bar{\Xi}^+$ )  $\approx$  92%.

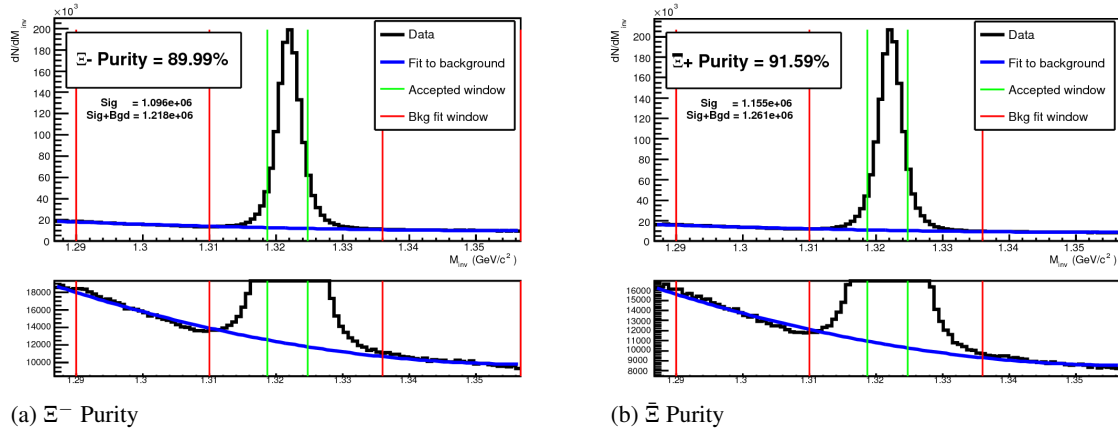


**Fig. 7:**  $\Xi^-$ ( $\bar{\Xi}^+$ ) Purity 0-10%: Purity( $\Xi^-$ )  $\approx$  90% and Purity( $\bar{\Xi}^+$ )  $\approx$  92%.

### 249 3.5 Pair Selection

250 It is important to obtain true particle pairs in the analysis. In particular, contamination from pairs con-  
251 structed with split or merged tracks, and pairs sharing daughters, can introduce an artificial signal into  
252 the correlation function, obscuring the actual physics.

#### 253 1. Shared Daughter Cut for Pairs

##### 254 (a) V0-V0 Pairs (i.e. $\Lambda(\bar{\Lambda})K_S^0$ analyses)

- Remove all pairs which share a daughter
    - Ex.  $\Lambda$  and  $K_S^0$  particles which share a  $\pi^-$  daughter are not included
- (b) V0-Track Pairs (i.e.  $\Lambda(\bar{\Lambda})K^\pm$  analyses)
- Remove pairs if Track is also used as a daughter of the V0
    - In these analyses, this could only occur if, for instance, a  $K$  is misidentified as a  $\pi$  or  $p$  in the V0 reconstruction
- (c)  $\Xi$ -Track Pairs
- Remove pairs if Track is also used as a daughter of the  $\Xi$ 
    - In these analyses, this could only occur if, for instance, a  $K$  is misidentified as a  $\pi$  or  $p$  in the V0 reconstruction, or misidentified as bachelor  $\pi$ .
  - Remove pair if bachelor  $\pi$  is also a daughter of the  $\Lambda$ 
    - This is not a pair cut, but is included here because this cut occurs in the AliFemtoXiTrackPairCut class

## 2. Average Separation Cuts

- Used to cut out splitting and merging effects
- The motivation for these cuts can be seen in Figures 8, 9, and 10, in which average separation correlation functions are presented

- (a)  $\Lambda(\bar{\Lambda})K_S^0$  Analyses
- Average separation  $> 6.0$  cm for like charge sign daughters
    - ex.  $p$  daughter of  $\Lambda$  and  $\pi^+$  daughter of  $K_S^0$
    - No cut for unlike-sign daughters
- (b)  $\Lambda(\bar{\Lambda})K^\pm$  Analyses
- Average Separation  $> 8.0$  cm for daughter of  $\Lambda(\bar{\Lambda})$  sharing charge sign of  $K^\pm$ 
    - ex. in  $\Lambda K^+$  analysis,  $p$  daughter of  $\Lambda$  with  $K^+$
    - No cut for unlike signs
- (c)  $\Xi(\bar{\Xi})K^\pm$  Analyses
- Average Separation  $> 8.0$  cm for any daughter of  $\Xi$  sharing charge sign of  $K^\pm$ 
    - ex. in  $\Xi^- K^-$  analysis,  $\pi^-$  daughter of  $\Lambda$  daughter with  $K^-$ , and bachelor  $\pi^-$  daughter with  $K^-$
    - No cut for unlike signs

## 4 Correlation Functions

This analysis studies the momentum correlations of both  $\Lambda$ - $K$  and  $\Xi$ - $K$  pairs using the two-particle correlation function, defined as  $C(k^*) = A(k^*)/B(k^*)$ , where  $A(k^*)$  is the signal distribution,  $B(k^*)$  is the reference (or background) distribution, and  $k^*$  is the momentum of one of the particles in the pair rest frame. In practice,  $A(k^*)$  is constructed by binning in  $k^*$  pairs from the same event. Ideally,  $B(k^*)$  is similar to  $A(k^*)$  in all respects excluding the presence of femtoscopic correlations [2]; as such,  $B(k^*)$  is used to divide out the phase-space effects, leaving only the femtoscopic effects in the correlation function.

In practice,  $B(k^*)$  is obtained by forming mixed-event pairs, i.e. particles from a given event are paired with particles from  $N_{mix} (= 5)$  other events, and these pairs are then binned in  $k^*$ . In forming the background distribution, it is important to mix only similar events; mixing events with different phase-spaces

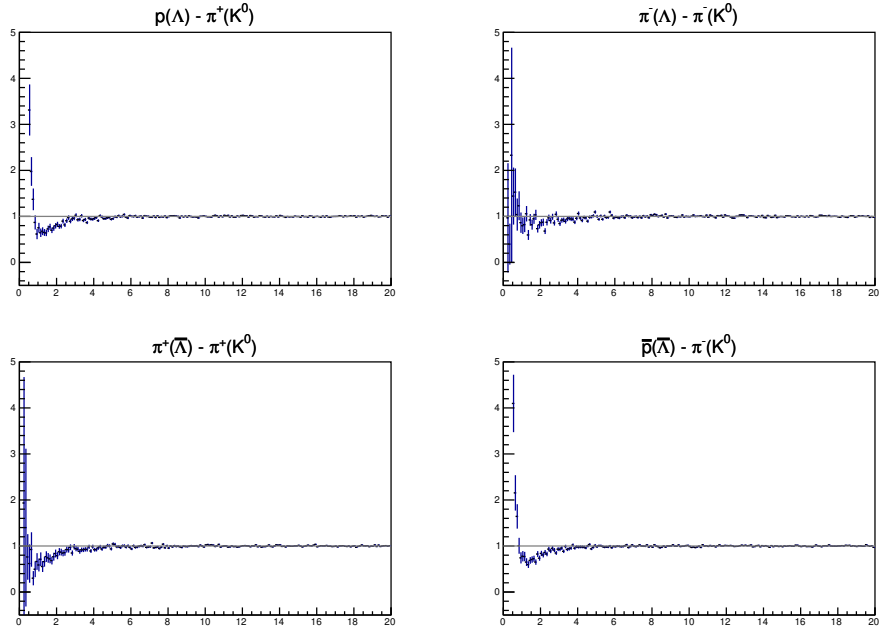


**Fig. 8:** Average separation (cm) correlation functions of  $\Lambda(\bar{\Lambda})$  and  $K_S^0$  Daughters. Only like-sign daughter pairs are shown (the distributions for unlike-signs were found to be flat). The title of each subfigure shows the daughter pair, as well as the mother of each daughter (in “()”), ex. top left is  $p$  from  $\Lambda$  with  $\pi^+$  from  $K_S^0$ .

295 can lead to artificial signals in the correlation function. Therefore, in this analysis, we mix events with  
 296 primary vertices within 2 cm and centralities within 5% of each other. Also note, a vertex correction is  
 297 also applied to each event, which essentially recenters the primary vertices to  $z = 0$ .

298 This analysis presents correlation functions for three centrality bins (0-10%, 10-30%, and 30-50%),  
 299 and is currently pair transverse momentum ( $k_T = 0.5|\mathbf{p}_{T,1} + \mathbf{p}_{T,2}|$ ) integrated (i.e. not binned in  $k_T$ ).  
 300 The correlation functions are constructed separately for the two magnetic field configurations, and are  
 301 combined using a weighted average:

$$C_{combined}(k^*) = \frac{\sum_i w_i C_i(k^*)}{\sum_i w_i} \quad (3)$$

302 where the sum runs over the correlation functions to be combined, and the weight,  $w_i$ , is the number of  
 303 numerator pairs in  $C_i(k^*)$ . Here, the sum is over the two field configurations.

304 Figures 11, 12, and 13 show the correlation functions for all centralities studied for  $\Lambda K_S^0(\bar{\Lambda} K_S^0)$ ,  $\Lambda K^+(\bar{\Lambda} K^-)$ ,  
 305 and  $\Lambda K^-(\bar{\Lambda} K^+)$ , respectively. All were normalized in the range  $0.32 < k^* < 0.4$  GeV/c.

## 306 5 Fitting

### 307 5.1 Model: $\Lambda K_S^0$ , $\Lambda K^\pm$ , $\Xi^{ch} K_S^0$

308 The two-particle relative momentum correlation function may be written theoretically by the Koonin-  
 309 Pratt equation [3, 4]:

$$C(\mathbf{k}^*) = \int S(\mathbf{r}^*) |\Psi_{\mathbf{k}^*}(\mathbf{r}^*)|^2 d^3 \mathbf{r}^* \quad (4)$$

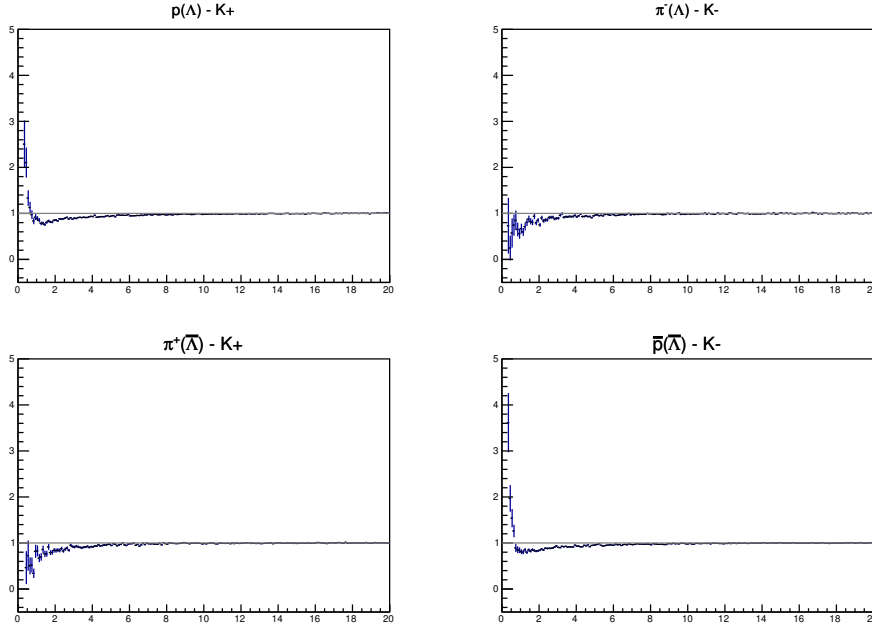


**Fig. 9:** Average separation (cm) correlation functions of  $\Lambda(\bar{\Lambda})$  Daughter and  $K^\pm$ . Only like-sign pairs are shown (unlike-signs were flat). In the subfigure titles, the particles in “()” represent the mothers, ex. top left is  $p$  from  $\Lambda$  with  $K^+$ .

310 In the absence of Coulomb effects, and assuming a spherically gaussian source of width  $R$ , the 1D  
 311 femtoscopic correlation function can be calculated analytically using:

$$C(k^*) = 1 + \lambda [C_{QI}(k^*) + C_{FSI}(k^*)] \quad (5)$$

312  $C_{QI}$  describes plane-wave quantum interference:

$$C_{QI}(k^*) = \alpha \exp(-4k^{*2}R^2) \quad (6)$$

313 where  $\alpha = (-1)^{2j}/(2j+1)$  for identical particles with spin  $j$ , and  $\alpha = 0$  for non-identical particles.  
 314 Obviously,  $\alpha = 0$  for all analyses presented in this note.  $C_{FSI}$  describes the s-wave strong final state  
 315 interaction between the particles:

$$\begin{aligned} C_{FSI}(k^*) &= (1 + \alpha) [\frac{1}{2} |\frac{f(k^*)}{R}|^2 (1 - \frac{d_0}{2\sqrt{\pi}R}) + \frac{2\mathbb{R}f(k^*)}{\sqrt{\pi}R} F_1(2k^*R) - \frac{\mathbb{I}f(k^*)}{R} F_2(2k^*R)] \\ f(k^*) &= (\frac{1}{f_0} + \frac{1}{2} d_0 k^{*2} - ik^*)^{-1}; \quad F_1(z) = \int_0^z \frac{e^{x^2-z^2}}{z} dx; \quad F_2(z) = \frac{1-e^{-z^2}}{z} \end{aligned} \quad (7)$$

316 where  $R$  is the source size,  $f(k^*)$  is the s-wave scattering amplitude,  $f_0$  is the complex scattering length,  
 317 and  $d_0$  is the effective range of the interaction.

318 The code developed to fit the data is called “LednickyFitter”, and utilizes the ROOT TMinuit implemen-  
 319 tation of the MINUIT fitting package. In short, given a function with a number of parameters, the fitter  
 320 explores the parameter space searching for the minimum of the equation. In this implementation, the  
 321 function to be minimized should represent the difference between the measure and theoretical corre-  
 322 lation functions. However, a simple  $\chi^2$  test is inappropriate for fitting correlation functions, as the ratio  
 323 two Poisson distributions does not result in a Poisson distribution. Instead, a log-likelihood fit function  
 324 of the following form is used [2]:

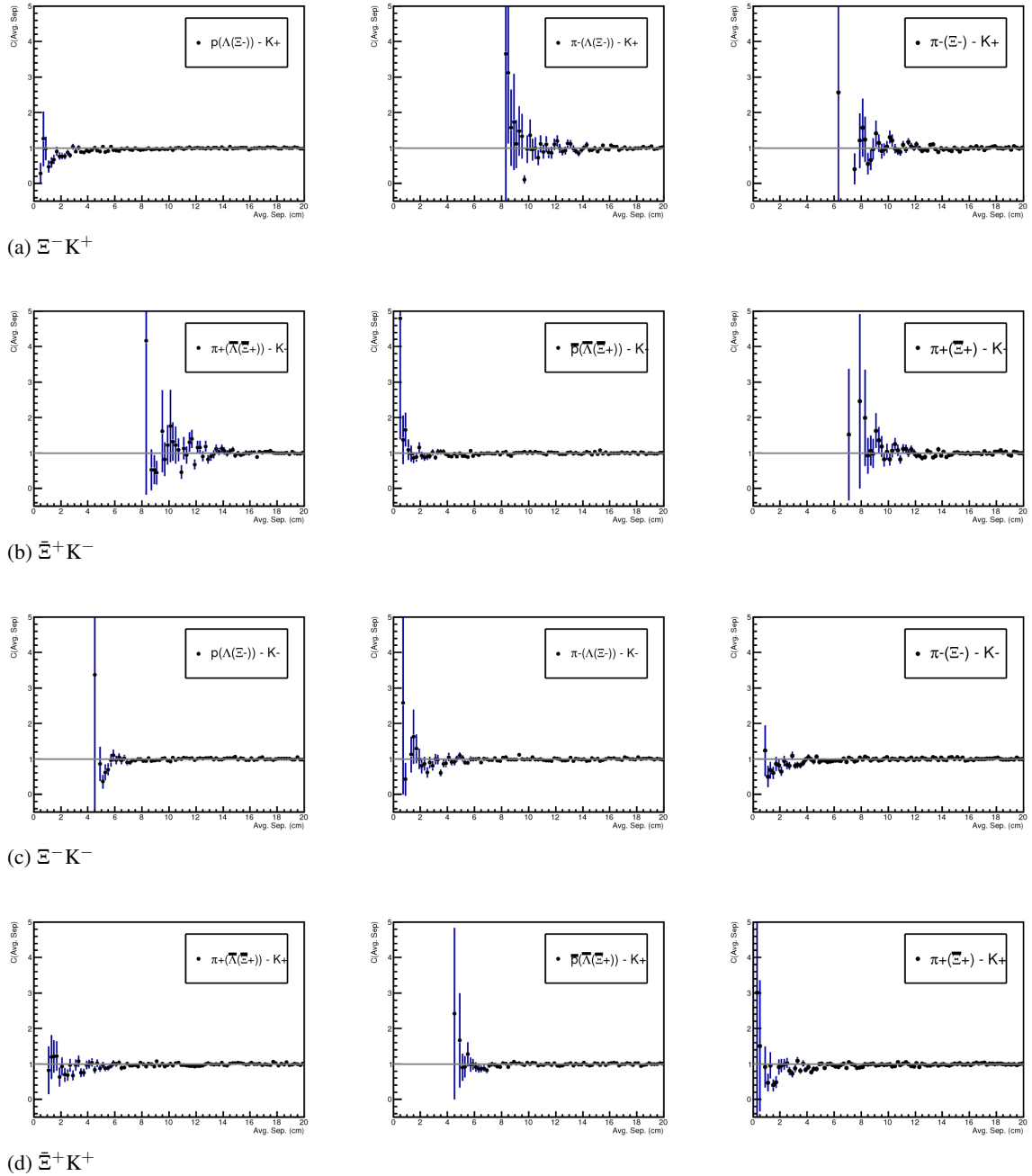


**Fig. 10:** Average separation (cm) correlation functions of  $\Xi$  Daughter and  $K^\pm$ . In the subfigure titles, the particles in “()” represent the mothers, ex. top left is  $p$  from  $\Lambda$  from  $\Xi^-$  with  $K^+$ .

$$\chi_{PML}^2 = -2 \left[ A \ln \left( \frac{C(A+B)}{A(C+1)} \right) + B \ln \left( \frac{A+B}{B(C+1)} \right) \right] \quad (8)$$

325 where  $A$  is the experimental signal distribution (numerator),  $B$  is the experimental background distribution  
326 (denominator), and  $C$  is the theoretical fit correlation function.

327 The LednickyFitter uses Equations 5 – 7 to build the theoretical fit, and Equation 8 as the statistic quantifying  
328 the quality of the fit. The parameters to be varied by MINUIT are:  $\lambda$ ,  $R$ ,  $f_0$  ( $\mathbb{R}f_0$  and  $\mathbb{I}f_0$  separately),  
329  $d_0$ , and normalization  $N$ . The fitter currently includes methods to correct for momentum resolution and  
330 a non-flat background. These corrections are applied to the fit function, the data is never touched. The

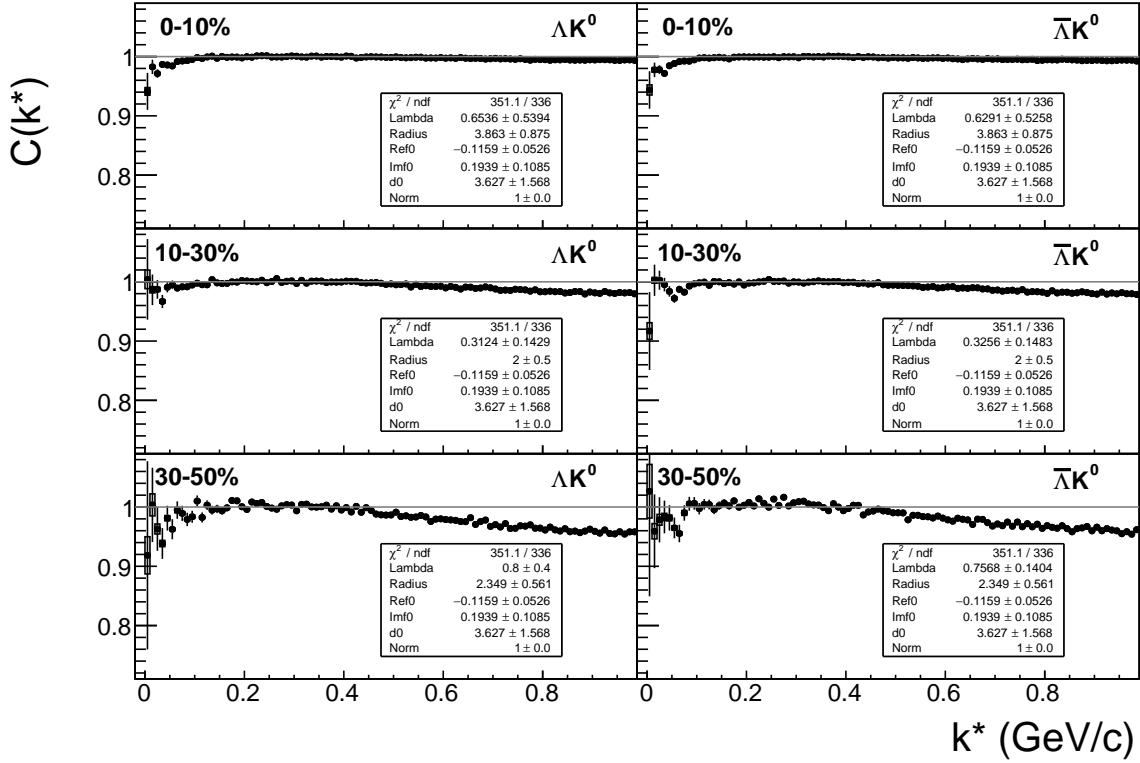


**Fig. 11:**  $\Lambda K_S^0$  (left) and  $\bar{\Lambda} K_S^0$  (right) correlation functions for 0-10% (top), 10-30% (middle), and 30-50% (bottom) centralities. The lines represent the statistical errors, while the boxes represent the systematic errors.

331 fitter is able to share parameters between different analyses and fit all simultaneously.  
 332 In a typical fit, a given pair is fit with its conjugate (ex.  $\Lambda K^+$  with  $\bar{\Lambda} K^-$ ) across all centralities (0-10%,  
 333 10-30%, 30-50%), for a total of 6 simultaneous analyses. Each analysis has a unique  $\lambda$  and normalization  
 334 parameter. The radii are shared between analyses of like centrality, as these should have similar source  
 335 sizes. The scattering parameters ( $\text{Ref}_0$ ,  $\text{Imf}_0$ ,  $d_0$ ) are shared amongst all.  
 336 Figures 19, 21, and 23 (Section 7) show experimental data with fits for all studied centralities for  $\Lambda K_S^0$   
 337 with  $\bar{\Lambda} K_S^0$ ,  $\Lambda K^+$  with  $\bar{\Lambda} K^-$ , and  $\Lambda K^-$  with  $\bar{\Lambda} K^+$ , respectively. In the figures, the black solid line repre-  
 338 sents the “raw” fit, i.e. not corrected for momentum resolution effects nor non-flat background. The  
 339 green line shows the fit to the non-flat background. The purple points show the fit after momentum res-  
 340 olution and non-flat background corrections have been applied. The initial values of the parameters is  
 341 listed, as well as the final fit values with uncertainties.

## 342 5.2 Model: $\Xi^{ch} K^{ch}$

343 When fitting the  $\Xi^-(\bar{\Xi}^+)K^\pm$  results, it is necessary to include both strong and Coulomb effects. In this  
 344 case, Equation 5 is no longer valid, and, in fact, there is no analytical form with which to fit. Therefore,  
 345 we must begin with the wave function describing the pair interaction, and simulate many particle pairs  
 346 to obtain a theoretical fit correlation function. The code developed to achieve this functionality is called  
 347 “CoulombFitter”. Currently, in order to generate the statistics needed for a stable fit, we find that  $\sim 10^4$   
 348 simulated pairs per 10 MeV bin are necessary. Unfortunately, the nature of this process means that the  
 349 “CoulombFitter” takes much longer to run than the “LednickyFitter” of Section 5.1.

350 The two-particle correlation function may be written as:

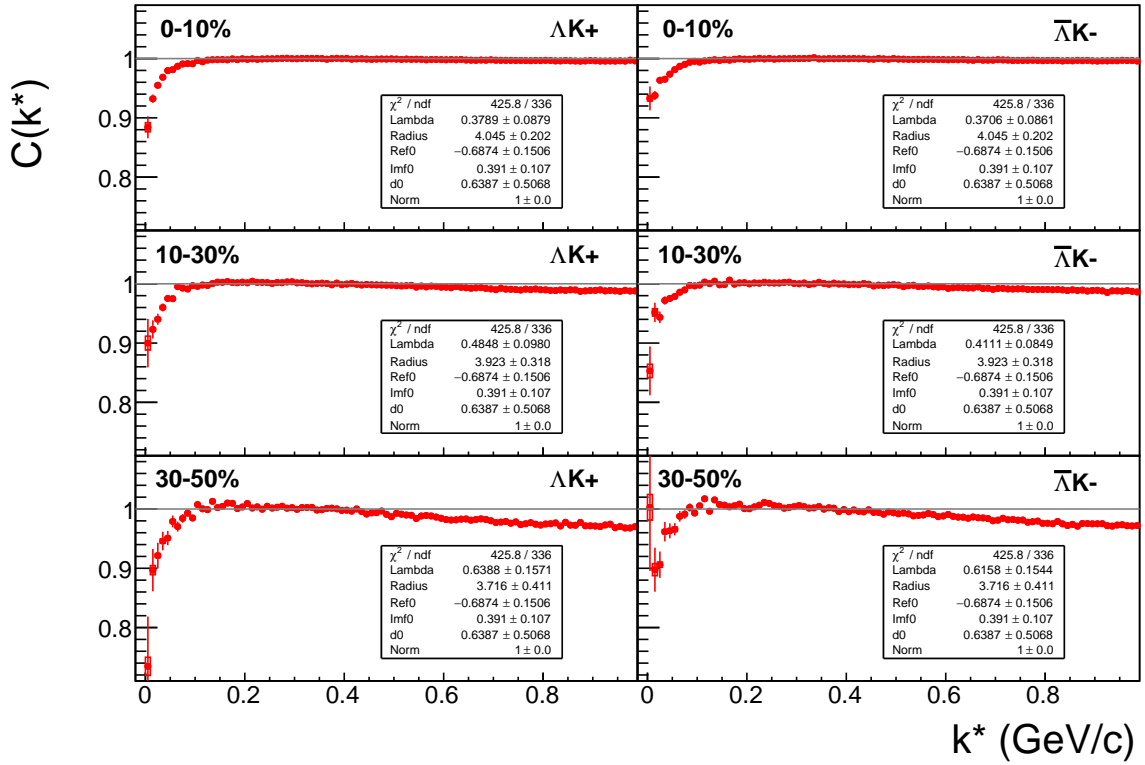


**Fig. 12:**  $\Lambda K^+$  (left) and  $\bar{\Lambda} K^-$  (right) correlation functions for 0-10% (top), 10-30% (middle), and 30-50% (bottom) centralities. The lines represent the statistical errors, while the boxes represent the systematic errors.

$$C(\mathbf{k}^*) = \sum_S \rho_S \int S(\mathbf{r}^*) |\Psi_{\mathbf{k}^*}^S(\mathbf{r}^*)|^2 d^3 \mathbf{r}^* \quad (9)$$

where  $\rho_S$  is the normalized emission probability of particles in a state with spin  $S$ ,  $S(\mathbf{r}^*)$  is the pair emission source distribution (assumed to be Gaussian), and  $\Psi_{\mathbf{k}^*}^S(\mathbf{r}^*)$  is the two-particle wave-function including both strong and Coulomb interactions [5]:

$$\Psi_{\mathbf{k}^*}(\mathbf{r}^*) = e^{i\delta_c} \sqrt{A_c(\eta)} [e^{i\mathbf{k}^* \cdot \mathbf{r}^*} F(-i\eta, 1, i\xi) + f_c(k^*) \frac{\tilde{G}(\rho, \eta)}{r^*}] \quad (10)$$

where  $\rho = k^* r^*$ ,  $\eta = (k^* a_c)^{-1}$ ,  $\xi = \mathbf{k}^* \cdot \mathbf{r}^* + k^* r^* \equiv \rho(1 + \cos \theta^*)$ , and  $a_c = (\mu z_1 z_2 e^2)^{-1}$  is the two-particle Bohr radius (including the sign of the interaction).  $\delta_c$  is the Coulomb s-wave phase shift,  $A_c(\eta)$  is the Coulomb penetration factor,  $\tilde{G} = \sqrt{A_c}(G_0 + iF_0)$  is a combination of the regular ( $F_0$ ) and singular ( $G_0$ ) s-wave Coulomb functions.  $f_c(k^*)$  is the s-wave scattering amplitude:

$$f_c(k^*) = [\frac{1}{f_0} + \frac{1}{2} d_0 k^{*2} - \frac{2}{a_c} h(\eta) - ik^* A_c(\eta)]^{-1} \quad (11)$$

where, the “h-function”,  $h(\eta)$ , is expressed through the digamma function,  $\psi(z) = \Gamma'(z)/\Gamma(z)$  as:

$$h(\eta) = 0.5[\psi(i\eta) + \psi(-i\eta) - \ln(\eta^2)] \quad (12)$$

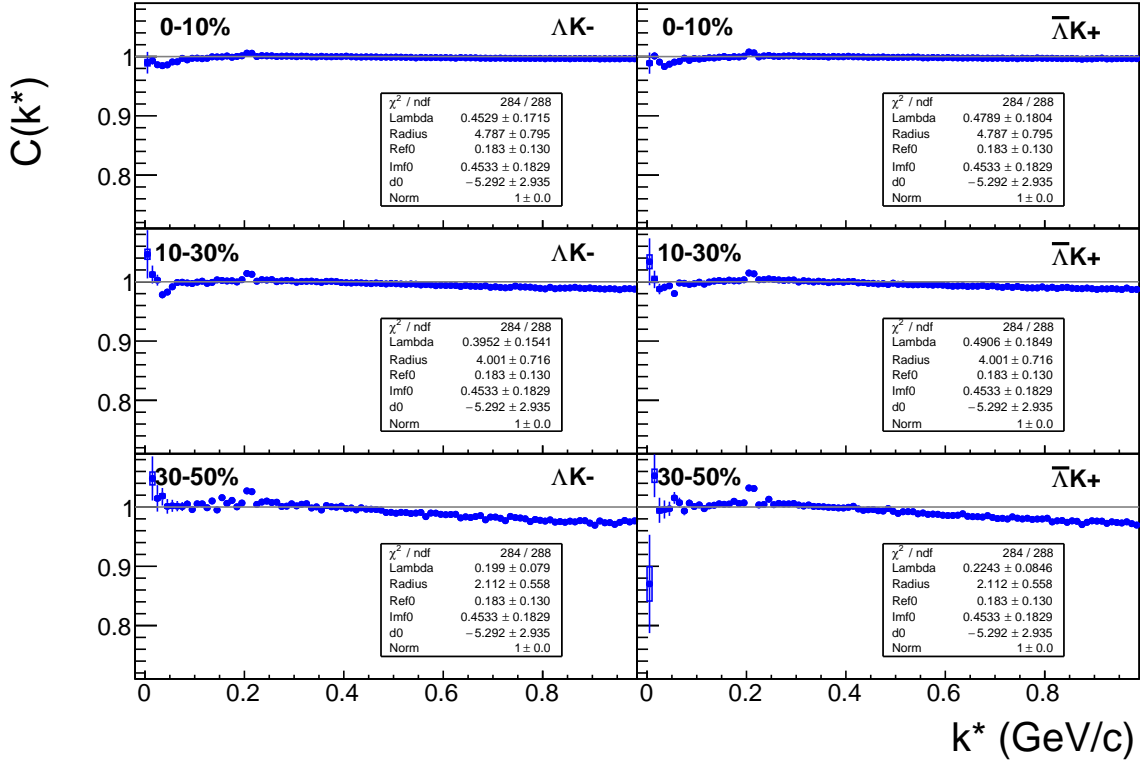


**Fig. 13:**  $\Lambda K^-$  (left) and  $\bar{\Lambda} K^+$  (right) correlation functions for 0-10% (top), 10-30% (middle), and 30-50% (bottom) centralities. The lines represent the statistical errors, while the boxes represent the systematic errors. The peak at  $k^* \approx 0.2$  GeV/c is due to the  $\Omega^-$  resonance.

Unfortunately, with this analysis, we are not sensitive to, and therefore not able to distinguish between, the iso-spin singlet and triplet states. We proceed with our analysis, but the results must be interpreted as iso-spin averaged scattering parameters.

As stated before, to generate a fit correlation function, we must simulate a large number of pairs, calculate the wave-function, and average  $\Psi^2$  over all pairs in a given  $k^*$  bin. Essentially, we calculate Equation 9 by hand:

$$\begin{aligned}
 C(\mathbf{k}^*) &= \sum_S \rho_S \int S(\mathbf{r}^*) |\Psi_{\mathbf{k}^*}^S(\mathbf{r}^*)|^2 d^3 \mathbf{r}^* \\
 &\rightarrow C(|\mathbf{k}^*|) \equiv C(k^*) = \sum_S \rho_S \langle |\Psi^S(\mathbf{k}_i^*, \mathbf{r}_i^*)|^2 \rangle_i \\
 &\rightarrow C(k^*) = \lambda \sum_S \rho_S \langle |\Psi^S(\mathbf{k}_i^*, \mathbf{r}_i^*)|^2 \rangle_i + (1 - \lambda)
 \end{aligned} \tag{13}$$

where  $\langle \rangle_i$  represents an average over all pairs in a given  $k^*$  bin.

In summary, for a given  $k^*$  bin, we must draw  $N_{pairs} \sim 10^4$  pairs, and for each pair:

- 367 1. Draw a random  $\mathbf{r}^*$  vector according to our Gaussian source distribution  $S(\mathbf{r}^*)$
- 368 2. Draw a random  $\mathbf{k}^*$  vector satisfying the  $|\mathbf{k}^*|$  restriction of the bin

369 – We draw from real  $k^*$  vectors obtained from the data

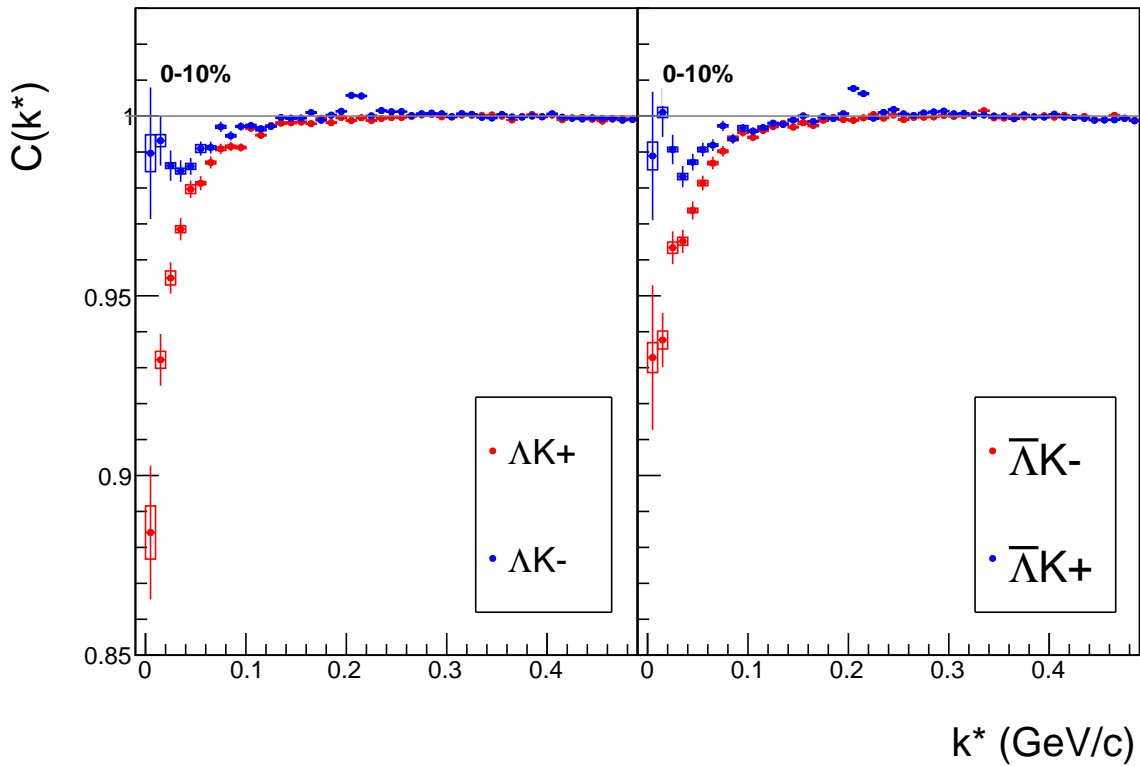


**Fig. 14:** Correlation Functions:  $\Lambda K^+$  vs  $\Lambda K^-$  ( $\bar{\Lambda} K^+$  vs  $\bar{\Lambda} K^-$ ) for 0-10% centrality. The peak in  $\Lambda K^- (\bar{\Lambda} K^+)$  at  $k^* \approx 0.2$  GeV/c is due to the  $\Omega^-$  resonance. The lines represent the statistical errors. (NOTE: This figure is slightly dated, and a new one will be generated which includes both statistical and systematic uncertainties)

370 – However, we find that drawing from a distribution flat in  $k^*$  gives similar results

371     3. Construct the wave-function  $\Psi$

372 After all pairs for a given  $k^*$  bin are simulated and wave-functions obtained, the results are averaged to  
373 give the fit result.

374 Construction of the wave-functions, Equation 10, involves a number of complex functions not included  
375 in standard C++ or ROOT libraries (namely,  $h(\eta)$ ,  $\tilde{G}(\rho, \eta)$ ), and  $F(-i\eta, 1, i\xi)$ . These functions were  
376 even difficult to find and implement from elsewhere. Our solution was to embed a Mathematica kernel  
377 into our C++ code to evaluate these functions. However, having Mathematica work on-the-fly with the  
378 fitter was far too time consuming (fitter would have taken day, maybe weeks to finish). Our solution  
379 was to use Mathematica to create matrices representing these functions for different parameter values.  
380 During fitting, these matrices were then interpolated and the results used to build the wave-functions.  
381 This method decreased the running time dramatically, and we are not able to generate results in under  $\sim$   
382 1 hour. This process will be explained in more detail in future versions of the note.

383     **5.3 Momentum Resolution Corrections**

384 Finite track momentum resolution causes the reconstructed momentum of a particle to smear around the  
385 true value. This, of course, also holds true for V0 particles. The effect is propagated up to the pairs  
386 of interest, which causes the reconstructed relative momentum ( $k_{Rec}^*$ ) to differ from the true momentum  
387 ( $k_{True}^*$ ). Smearing of the momentum typically will result in a suppression of the signal.

388 The effect of finite momentum resolution can be investigated using the MC data, for which both the true

and reconstructed momenta are available. Figure 15 shows sample  $k_{True}^*$  vs.  $k_{Rec}^*$  plots for  $\Lambda(\bar{\Lambda})K^\pm$  0-10% analyses; Figure 15a was generated using same-event pairs, while Figure 15b was generated using mixed-event pairs (with  $N_{mix} = 5$ ).

If there are no contaminations in our particle collection, the plots in Figure 15 should be smeared around  $k_{True}^* = k_{Rec}^*$ ; this is mostly true in our analyses. However, there are some interesting features of our results which demonstrate a small (notice the log-scale on the z-axis) contamination in our particle collection. The structure around  $k_{Rec}^* = k_{True}^* - 0.15$  is mainly caused by  $K_S^0$  contamination in our  $\Lambda(\bar{\Lambda})$  sample. The remaining structure not distributed about  $k_{Rec}^* = k_{True}^*$  is due to  $\pi$  and  $e$  contamination in our  $K^\pm$  sample. These contaminations are more visible in Figure 16, which show  $k_{Rec}^*$  vs.  $k_{True}^*$  plots (for a small sample of the  $\Lambda K^\pm$  0-10% central analysis), for which the MC truth (i.e. true, known identity of the particle) was used to eliminate misidentified particles in the  $K^+$ (a) and  $\Lambda$ (b) collections. (NOTE: This is an old figure and is for a small sample of the data. A new version will be generated shortly. It, nonetheless, demonstrates the point well).

Information gained from looking at  $k_{Rec}^*$  vs  $k_{True}^*$  can be used to apply corrections to account for the effects of finite momentum resolution on the correlation functions. A typical method involves using the MC HIJING data to build two correlation functions,  $C_{Rec}(k^*)$  and  $C_{True}(k^*)$ , using the generator-level momentum ( $k_{True}^*$ ) and the measured detector-level momentum ( $k_{Rec}^*$ ). The data is then corrected by multiplying by the ratio,  $C_{True}/C_{Rec}$ , before fitting. This essentially unsmears the data, which that can be compared directly to theoretical predictions and fits. Although this is conceptually simple, there are a couple of big disadvantages to this method. First, HIJING does not incorporate final-state interactions, so weights must be used when building same-event (numerator) distributions. These weights account for the interactions, and, in the absence of Coulomb interactions, can be calculated using Eq. 5. Of course, these weights are valid only for a particular set of fit parameters. Therefore, in the fitting process, during which the fitter explores a large parameter set, the corrections will not remain valid. As such, applying the momentum resolution correction and fitting becomes a long and drawn out iterative process. An initial parameter set is obtained (through fitting without momentum resolution corrections, theoretical models, or a good guess), then the MC data is run over to obtain the correction factor, the data is fit using the correction factor, a refined parameter set is extracted, the MC data is run over again to obtain the new correction factor, etc. This process continues until the parameter set stabilizes. The second issue concerns statistics. With the MC data available on the grid, we were not able to generate the statistics necessary to use the raw  $C_{True}/C_{Rec}$  ratio. The ratio was not stable, and when applied to the data, obscured the signal. Attempting to fit the ratio to generate the corrections also proved problematic. However, as HIJING does not include final-state interactions, the same-event and mixed-event pairs are very similar (with the exception of things like energy and momentum conservation, etc). Therefore, one may build the numerator distribution using mixed-event pairs. This corresponds, more or less, to simply running a weight generator through the detector framework.

A second approach is to use information gained from plots like those in Figure 15, which can be considered response matrices. The response matrix describes quantitatively how each  $k_{Rec}^*$  bin receives contributions from multiple  $k_{True}^*$  bins, and can be used to account for the effects of finite momentum resolution. With this approach, the resolution correction is applied on-the-fly during the fitting process by propagating the theoretical (fit) correlation function through the response matrix, according to:

$$C_{fit}(k_{Rec}^*) = \frac{\sum_{k_{True}^*} M_{k_{Rec}^*, k_{True}^*} C_{fit}(k_{True}^*)}{\sum_{k_{True}^*} M_{k_{Rec}^*, k_{True}^*}} \quad (14)$$

where  $M_{k_{Rec}^*, k_{True}^*}$  is the response matrix (Figure 15),  $C_{fit}(k_{True}^*)$  is the fit binned in  $k_{True}^*$ , and the denominator normalizes the result.

432 Equation 14 describes that, for a given  $k_{Rec}^*$  bin, the observed value of  $C(k_{Rec}^*)$  is a weighted average of  
 433 all  $C(k_{True}^*)$  values, where the weights are the normalized number of counts in the  $[k_{Rec}^*, k_{True}^*]$  bin. As  
 434 seen in Figure 15, overwhelmingly the main contributions comes from the  $k_{Rec}^* = k_{True}^*$  bins. Although  
 435 the correction is small, it is non-negligible for the low- $k^*$  region of the correlation function.

436 Here, the momentum resolution correction is applied to the fit, not the data. In other words, during  
 437 fitting, the theoretical correlation function is smeared just as real data would be, instead of unsmearing  
 438 the data. This may not be ideal for the theorist attempting to compare a model to experimental data, but  
 439 it leaves the experimental data unadulterated. The current analyses use this second approach to applying  
 440 momentum resolution corrections because of two major advantages. First, the MC data must be analyzed  
 441 only once, and no assumptions about the fit are needed. Secondly, the momentum resolution correction  
 442 is applied on-the-fly by the fitter, delegating the iterative process to a computer instead of the user.

#### 443 5.4 Residual Correlations

444 The purpose of this analysis is study the interaction and scale of the emitting source of the pairs. In order  
 445 to obtain correct results, it is important for our particle collections to consist of primary particles. In  
 446 practice, this is difficult to achieve for our  $\Lambda$  and  $\bar{\Lambda}$  collections. Many of our  $\Lambda$  particles are not primary,  
 447 but originate as decay products from other hyperons, including  $\Sigma^0$ ,  $\Xi^-$ ,  $\Xi^0$  and  $\Omega^-$ . In these decays,  
 448 the  $\Lambda$  carries away a momentum very similar to that of its parent. As a result, the correlation function  
 449 between a secondary  $\Lambda$  and, for instance, a  $K^+$  will be sensitive to, and dependent upon, the interaction  
 450 between the parent of the  $\Lambda$  and the  $K^+$ . In effect, the correlation between the parent of the  $\Lambda$  and the  $K^+$   
 451 (ex.  $\Sigma^0 K^+$ ) will be visible, although smeared out, in the  $\Lambda K^+$  data. We call this a residual correlation  
 452 resulting from feed-down.

453 As it is difficult for us to eliminate these residual correlations in our analyses, we must attempt to account  
 454 for them in our fitter. To achieve this, we will simultaneously fit the data for both the primary correlation  
 455 function and the residual correlations. For example, in the simple case of a  $\Lambda K^+$  analysis with residuals  
 456 arising solely from  $\Sigma^0 K^+$  feed-down:

$$C_{measured}(k_{\Lambda K^+}^*) = 1 + \lambda_{\Lambda K^+}[C_{\Lambda K^+}(k_{\Lambda K^+}^*) - 1] + \lambda_{\Sigma^0 K^+}[C_{\Sigma^0 K^+}(k_{\Lambda K^+}^*) - 1]$$

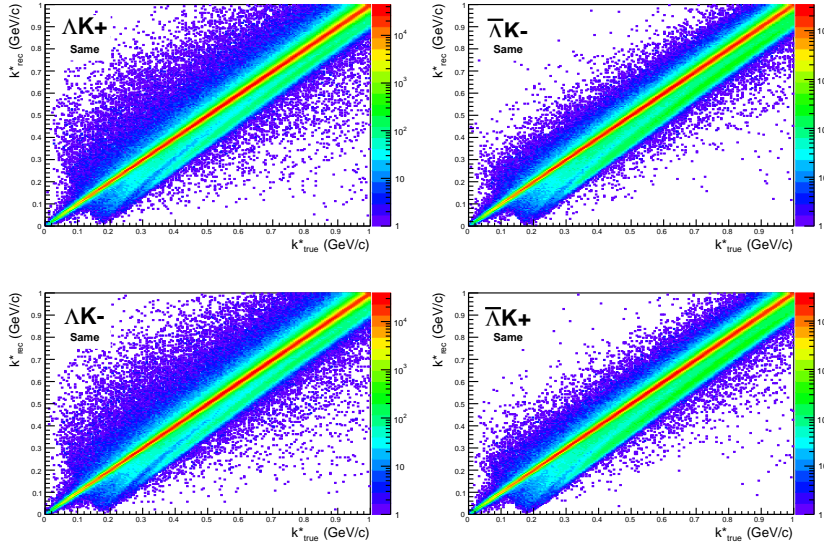
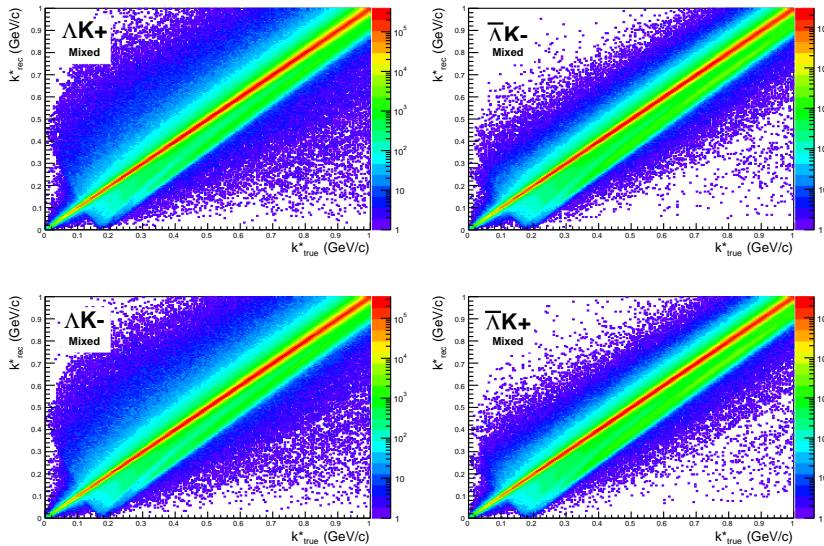
$$C_{\Sigma^0 K^+}(k_{\Lambda K^+}^*) \equiv \sum_{k_{\Sigma^0 K^+}^*} \frac{C_{\Sigma^0 K^+}(k_{\Sigma^0 K^+}^*) T(k_{\Sigma^0 K^+}^*, k_{\Lambda K^+}^*)}{T(k_{\Sigma^0 K^+}^*, k_{\Lambda K^+}^*)} \quad (15)$$

457  $C_{\Sigma^0 K^+}(k_{\Sigma^0 K^+}^*)$  is the  $\Sigma^0 K^+$  correlation function from, for instance, Equation 5, and  $T$  is the transform  
 458 matrix generated with THERMINATOR. This equation can be easily extended to include feed-down  
 459 from more sourced:

$$C_{measured}(k_{\Lambda K}^*) = \sum_i \lambda_i C_i(k_{\Lambda K}^*) \quad (16)$$

460 The framework for extracting the necessary transform matrices from the THERMINATOR data is already  
 461 in place, and has been used to generate the examples from  $\Lambda K^+$  and  $\bar{\Lambda} K^+$  analyses shown in Figures 17  
 462 and 18. However, these residual correlations have not yet been implemented in the fitter.

463 There is an obvious added complication here, as, for instance, the  $\Xi^- K^\pm$  residuals necessitate the in-  
 464 clusion of the CoulombFitter into the process. The complication of combining the two fitters is not as  
 465 troubling as the increase in fitting time that this is sure to bring. Additionally, in the future, we may  
 466 combine our  $\Lambda K$  and  $\Xi K$  analyses to be fit simultaneously.

(a) Same Event Pairs ( $\Lambda(\bar{\Lambda})K^\pm$ , 0-10% Centrality)(b) Mixed Event Pairs ( $\Lambda(\bar{\Lambda})K^\pm$ , 0-10% Centrality)

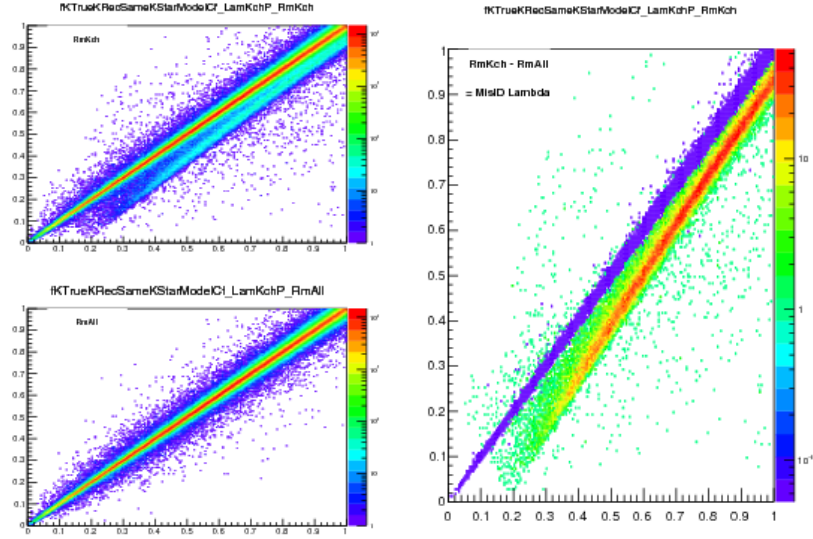
**Fig. 15:** Sample  $k_{True}^*$  vs.  $k_{Rec}^*$  plot for  $\Lambda(\bar{\Lambda})K^\pm$  0-10% analyses. The structure which appears around  $k_{Rec}^* = k_{True}^* - 0.15$  is mainly caused by  $K_S^0$  contamination in our  $\Lambda(\bar{\Lambda})$  sample. The remaining structure not distributed about  $k_{Rec}^* = k_{True}^*$  is due to  $\pi$  and  $e$  contamination in our  $K^\pm$  sample. These contaminations are more clearly visible in Figure 16

## 467 6 Systematic Errors

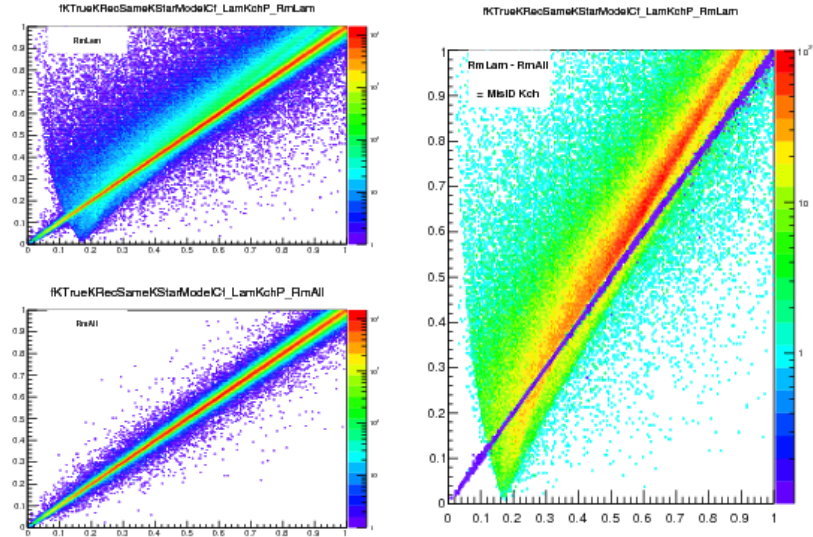
468 In order to understand my systematic uncertainties, the analysis code was run many times using slightly  
469 different values for a number of important cuts, and the results were compared.

470 In order to quantify the systematic errors on the data, all correlation functions built using all varied cut  
471 values were bin-by-bin averaged, and the resulting variance of each bin was taken as the systematic error.  
472 The cuts which were utilized in this study are presented in Sections 6.1.1 ( $\Lambda K_S^0$ ) and 6.2.1 ( $\Lambda K^\pm$ ).

473 Similarly, the fit parameters extracted from all of these correlation functions were averaged, and the  
474 resulting variances were taken as the systematic errors for the fit parameters. As with the systematic



(a) (Top Left) All misidentified  $K^+$  excluded. (Bottom Left) All misidentified  $\Lambda$  and  $K^+$  excluded. (Right) The difference of (Top Left) - (Bottom Left), which reveals the contamination in our  $\Lambda$  collection. The structure which appears around  $k_{Rec}^* = k_{True}^* - 0.15$  is mainly caused by  $K_S^0$  contamination in our  $\Lambda(\bar{\Lambda})$  sample.



(b) (Top Left) All misidentified  $\Lambda$  excluded. (Bottom Left) All misidentified  $\Lambda$  and  $K^+$  excluded. (Right) The difference of (Top Left) - (Bottom Left), which reveals the contamination in our  $K^+$  collection. The structure not distributed about  $k_{Rec}^* = k_{True}^*$  is due to  $\pi$  and  $e^-$  contamination in our  $K^\pm$  sample.

**Fig. 16:** Note: This is an old figure and is for a small sample of the data. A new version will be generated shortly.  
 $y\text{-axis} = k_{Rec}^*$ ,  $x\text{-axis} = k_{True}^*$ .

(Left)  $k_{Rec}^*$  vs.  $k_{True}^*$  plots for a small sample of the  $\Lambda K^+$  0-10% central analysis, MC truth was used to eliminate misidentified particles in the  $K^+$ (a) and  $\Lambda$ (b) collections. (Right) The difference of the top left and bottom left plots. Contaminations in our particle collections are clearly visible. Figure (a) demonstrates a  $K_S^0$  contamination in our  $\Lambda$  collection; Figure (b) demonstrates a  $\pi$  and  $e^-$  contamination in our  $K^\pm$  collection.

475 errors on the data, this was performed for all varied cut values. Additionally, a systematic analysis was  
476 done on our fit method (which, for now, just includes our choice of fit range). These two sources of  
477 uncertainty were combined in quadrature to obtain the final systematic uncertainties on the extracted fit

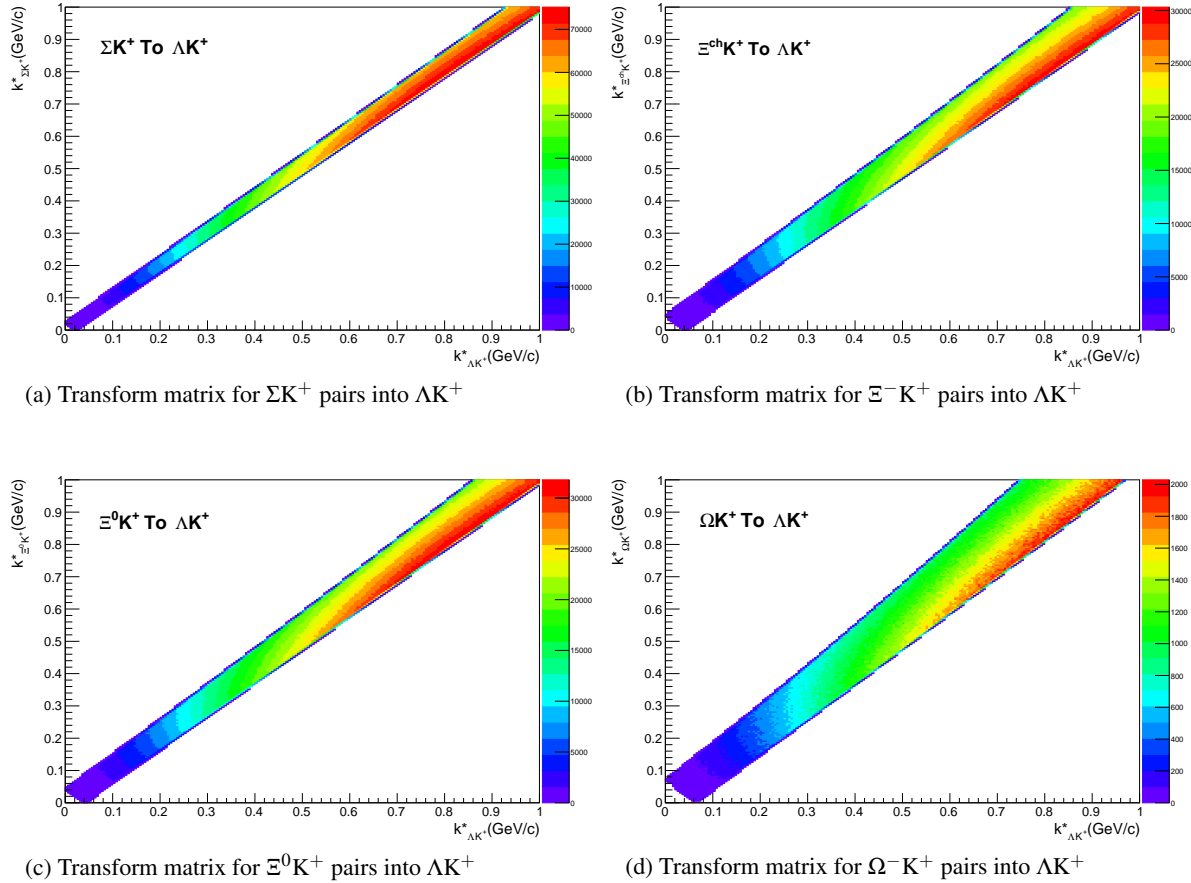


**Fig. 17:** Transform Matrices generated with THERMINATOR for  $\Lambda K^+$  Analysis

478 parameters.

479 **6.1 Systematic Errors:  $\Lambda K_S^0$**

480 **6.1.1 Particle and Pair Cuts**

481 The cuts included in the systematic study, as well as the values used in the variations, are listed below.  
482 Note, the central value corresponds to that used in the analysis.

- 483 1. DCA  $\Lambda(\bar{\Lambda})$ : {4, 5, 6 mm}
- 484 2. DCA  $K_S^0$ : {2, 3, 4 mm}
- 485 3. DCA  $\Lambda(\bar{\Lambda})$  Daughters: {3, 4, 5 mm}
- 486 4. DCA  $K_S^0$  Daughters: {2, 3, 4 mm}
- 487 5.  $\Lambda(\bar{\Lambda})$  Cosine of Pointing Angle: {0.9992, 0.9993, 0.9994}
- 488 6.  $K_S^0$  Cosine of Pointing Angle: {0.9992, 0.9993, 0.9994}
- 489 7. DCA to Primary Vertex of  $p(\bar{p})$  Daughter of  $\Lambda(\bar{\Lambda})$ : {0.5, 1, 2 mm}
- 490 8. DCA to Primary Vertex of  $\pi^-(\pi^+)$  Daughter of  $\Lambda(\bar{\Lambda})$ : {2, 3, 4 mm}
- 491 9. DCA to Primary Vertex of  $\pi^+$  Daughter of  $K_S^0$ : {2, 3, 4 mm}

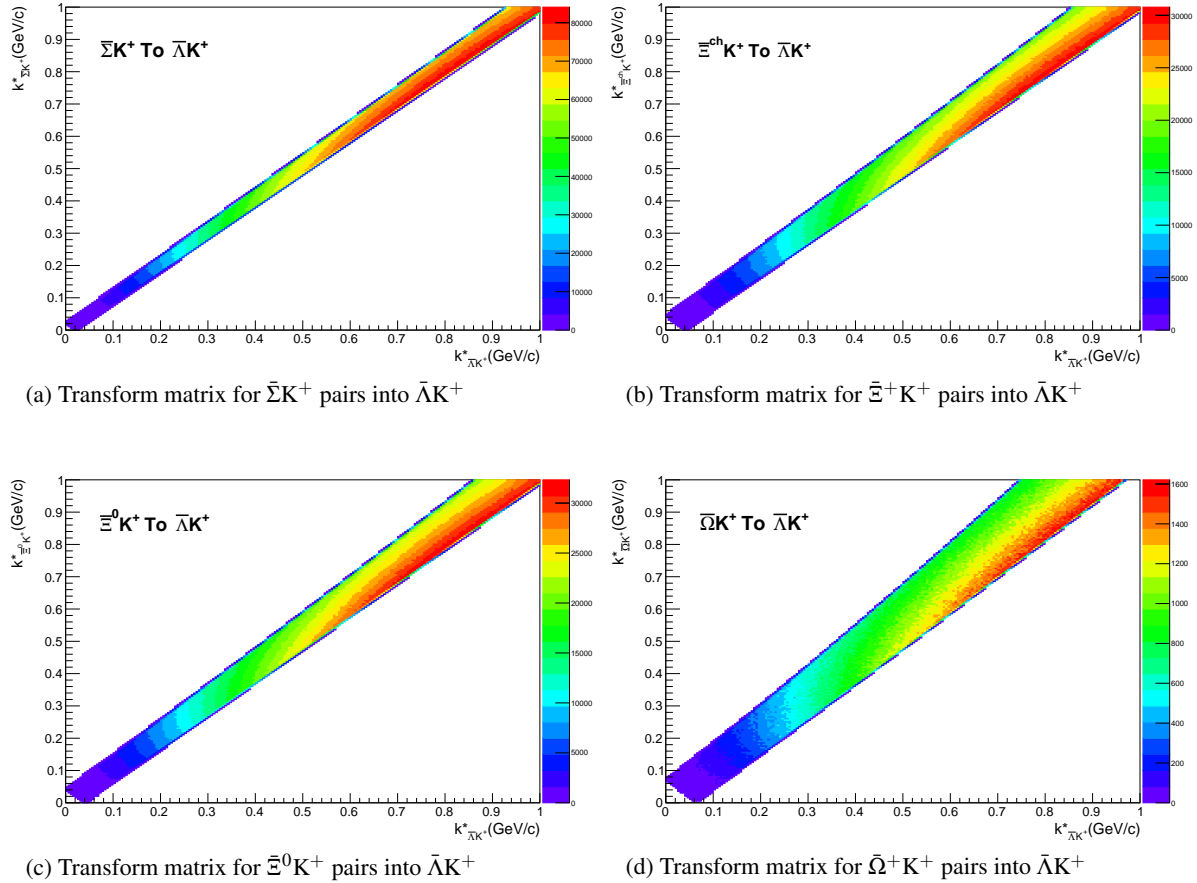


**Fig. 18:** Transform Matrices generated with THERMINATOR for  $\bar{\Lambda}K^+$  Analysis

492 10. DCA to Primary Vertex of  $\pi^-$  Daughter of  $K_S^0$ : {2, 3, 4 mm}

493 11. Average Separation of Like-Charge Daughters: {5, 6, 7 cm}

494 **6.1.2 Non-Flat Background**

495 We fit our non-flat background with a linear function. To study the contribution of this choice to our sys-  
496 tematic errors, we also fit with a quadratic and Gaussian form. The resulting uncertainties are combined  
497 with the uncertainties arising from our particle cuts.

498 **6.1.3 Fit Range**

499 Our choice of  $k^*$  fit range was varied by  $\pm 25\%$ . The resulting uncertainties in the extracted parameter  
500 sets were combined with our uncertainties arising from our particle and pair cuts.

501 **6.2 Systematic Errors:  $\Lambda K^\pm$**

502 **6.2.1 Particle and Pair Cuts**

503 The cuts included in the systematic study, as well as the values used in the variations, are listed below.  
504 Note, the central value corresponds to that used in the analysis.

505 1. DCA  $\Lambda(\bar{\Lambda})$ : {4, 5, 6 mm}

- 506    2. DCA  $\Lambda(\bar{\Lambda})$  Daughters: {3, 4, 5 mm}
- 507    3.  $\Lambda(\bar{\Lambda})$  Cosine of Pointing Angle: {0.9992, 0.9993, 0.9994}
- 508    4. DCA to Primary Vertex of  $p(\bar{p})$  Daughter of  $\Lambda(\bar{\Lambda})$ : {0.5, 1, 2 mm}
- 509    5. DCA to Primary Vertex of  $\pi^-(\pi^+)$  Daughter of  $\Lambda(\bar{\Lambda})$ : {2, 3, 4 mm}
- 510    6. Average Separation of  $\Lambda(\bar{\Lambda})$  Daughter with Same Charge as  $K^\pm$ : {7, 8, 9 cm}
- 511    7. Max. DCA to Primary Vertex in Transverse Plane of  $K^\pm$ : {1.92, 2.4, 2.88}
- 512    8. Max. DCA to Primary Vertex in Longitudinal Direction of  $K^\pm$ : {2.4, 3.0, 3.6}

513 **6.2.2 Non-Flat Background**

514 We fit our non-flat background with a linear function. To study the contribution of this choice to our sys-  
 515 tematic errors, we also fit with a quadratic and Gaussian form. The resulting uncertainties are combined  
 516 with the uncertainties arising from our particle cuts.

517 **6.2.3 Fit Range**

518 Our choice of  $k^*$  fit range was varied by  $\pm 25\%$ . The resulting uncertainties in the extracted parameter  
 519 sets were combined with our uncertainties arising from our particle and pair cuts.

520 **6.3 Systematic Errors:  $\Xi K^\pm$**

521 **6.3.1 Particle and Pair Cuts**

522 The cuts included in the systematic study, as well as the values used in the variations, are listed below.  
 523 Note, the central value corresponds to that used in the analysis.

- 524    1. Max. DCA  $\Xi(\bar{\Xi})$ : {x, y, z mm}
- 525    2. Max. DCA  $\Xi(\bar{\Xi})$  Daughters: {x, y, z mm}
- 526    3. Min.  $\Xi(\bar{\Xi})$  Cosine of Pointing Angle to Primary Vertex: {0.9991, 0.9992, 0.9993}
- 527    4. Min.  $\Lambda(\bar{\Lambda})$  Cosine of Pointing Angle to  $\Xi(\bar{\Xi})$  Decay Vertex: {0.9992, 0.9993, 0.9994}
- 528    5. Min. DCA Bachelor  $\pi$ : {0.2, 0.3, 0.4 mm}
- 529    6. Min. DCA  $\Lambda(\bar{\Lambda})$ : {0.5, 1, 2 mm}
- 530    7. Max. DCA  $\Lambda(\bar{\Lambda})$  Daughters: {3, 4, 5 mm}
- 531    8. Min.  $\Lambda(\bar{\Lambda})$  Cosine of Pointing Angle To Primary Vertex: {0.9992, 0.9993, 0.9994}
- 532    9. Min. DCA to Primary Vertex of  $p(\bar{p})$  Daughter of  $\Lambda(\bar{\Lambda})$ : {0.5, 1, 2 mm}
- 533    10. Min. DCA to Primary Vertex of  $\pi^-(\pi^+)$  Daughter of  $\Lambda(\bar{\Lambda})$ : {2, 3, 4 mm}
- 534    11. Min. Average Separation of  $\Lambda(\bar{\Lambda})$  Daughter and  $K^\pm$  with like charge: {7, 8, 9 cm}
- 535    12. Min. Average Separation of Bachelor  $\pi$  and  $K^\pm$  with like charge: {x, y, z cm}
- 536    13. Max. DCA to Primary Vertex in Transverse Plane of  $K^\pm$ : {1.92, 2.4, 2.88}
- 537    14. Max. DCA to Primary Vertex in Longitudinal Direction of  $K^\pm$ : {2.4, 3.0, 3.6}

538 **7 Results and Discussion**

539 **7.1 Results:  $\Lambda K_S^0$  and  $\Lambda K^\pm$**

540 Figures 19, 21, and 23 (Section 7) show experimental data with fits for all studied centralities for  $\Lambda K_S^0$   
541 with  $\bar{\Lambda} K_S^0$ ,  $\Lambda K^+$  with  $\bar{\Lambda} K^-$ , and  $\Lambda K^-$  with  $\bar{\Lambda} K^+$ , respectively. The parameter sets extracted from the fits  
542 can be found in Tables 1 and 2. All correlation functions were normalized in the range  $0.32 < k^* < 0.40$   
543 GeV/c, and fit in the range  $0.0 < k^* < 0.30$  GeV/c. For the  $\Lambda K^-$  and  $\bar{\Lambda} K^+$  analyses, the region  $0.19$   
544  $< k^* < 0.23$  GeV/c was excluded from the fit to exclude the bump caused by the  $\Omega^-$  resonance. The  
545 non-flat background was fit with a linear form from  $0.6 < k^* < 0.9$  GeV/c. The theoretical fit function  
546 was then multiplied by this background during the fitting process.

547 In the figures (19, 21, and 23), the black solid line represents the “raw” fit, i.e. not corrected for momen-  
548 tum resolution effects nor non-flat background. The green line shows the fit to the non-flat background.  
549 The purple points show the fit after momentum resolution and non-flat background corrections have been  
550 applied. The initial values of the parameters is listed, as well as the final fit values with uncertainties.

551 For the  $\Lambda K_S^0$  fits,  $R$  was restricted to [2.0, 10.0 fm] and  $\Lambda$  was restricted to [0.1, 0.8]. This gave the lowest  
552  $\chi^2$  value, but loosening this restriction changes the fit parameters slightly. Notice, the 10-30% radius is  
553 at its limit, as is  $\lambda$  from the 30-50%  $\Lambda K_S^0$  analysis. This accounts for the 0.000 systematic uncertainty of  
554 the 10-30%  $R$  value currently quoted in Table 1. An estimate for this uncertainty should be included in  
555 the next version of this note. In the future, we may need to throw out the 30-50% data from the fit, but  
556 this is not ideal.

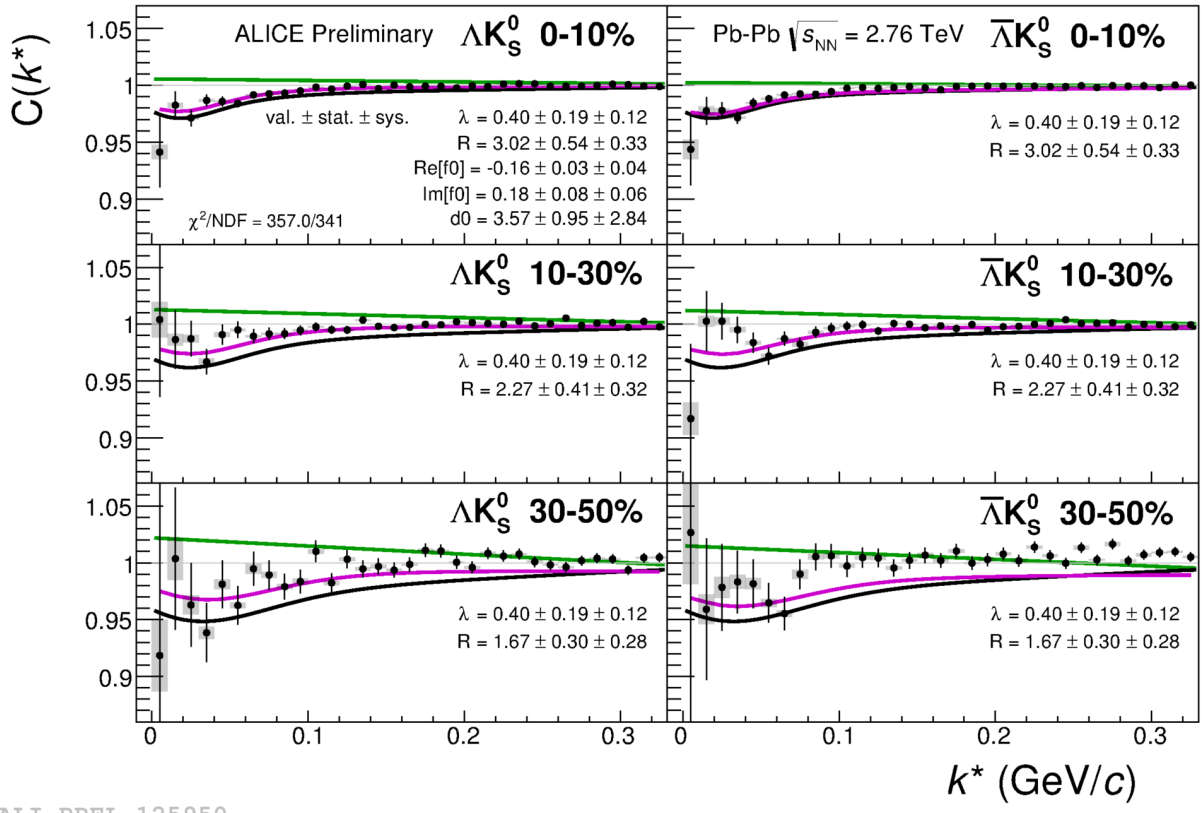


**Fig. 19:** Fits to the  $\Lambda K_S^0$  (left) and  $\bar{\Lambda} K_S^0$  (right) data for the centralities 0-10% (top), 10-30% (middle), and 30-50% (bottom). The lines represent the statistical errors, while the boxes represent the systematic errors. Each has unique  $\lambda$  and normalization parameters. The radii are shared amongst like centralities; the scattering parameters ( $R f_0$ ,  $\Re f_0$ ,  $d_0$ ) are shared amongst all. The black solid line represents the “raw” fit, i.e. not corrected for momentum resolution effects nor non-flat background. The green line shows the fit to the non-flat background. The purple points show the fit after momentum resolution and non-flat background corrections have been applied. The initial values of the parameters is listed, as well as the final fit values with uncertainties. Here,  $R$  was restricted to [2.,10.] and  $\Lambda$  was restricted to [0.1,0.8].

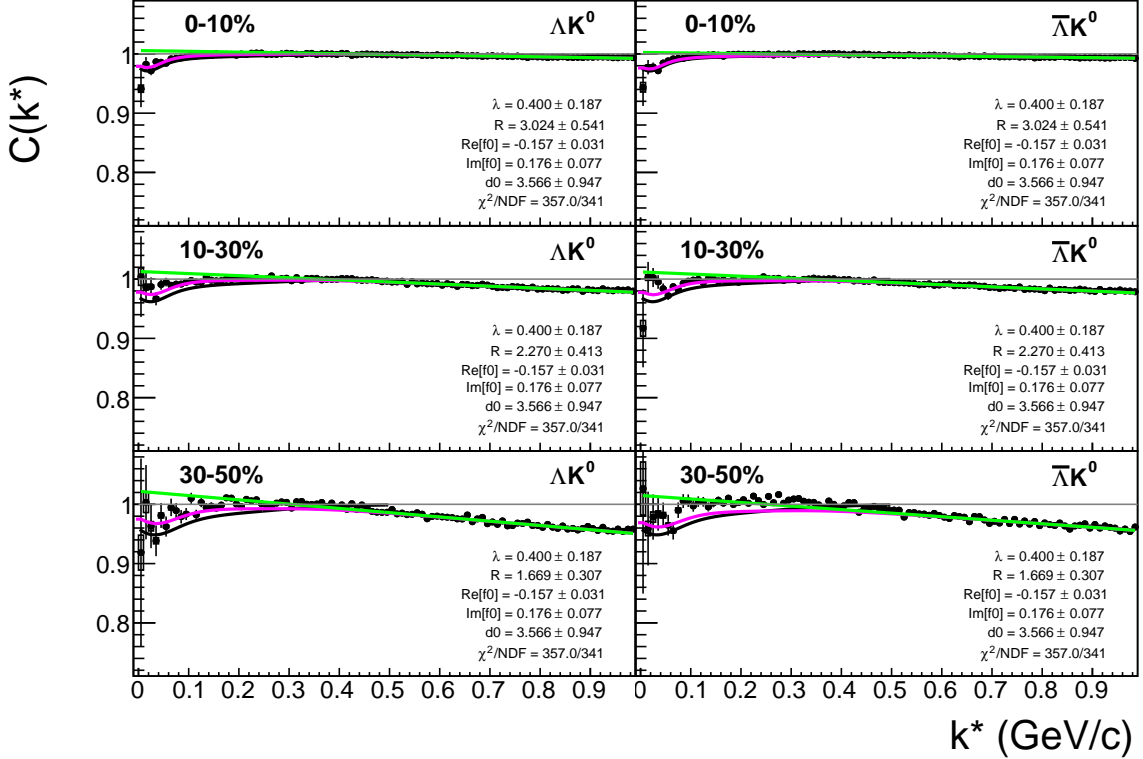
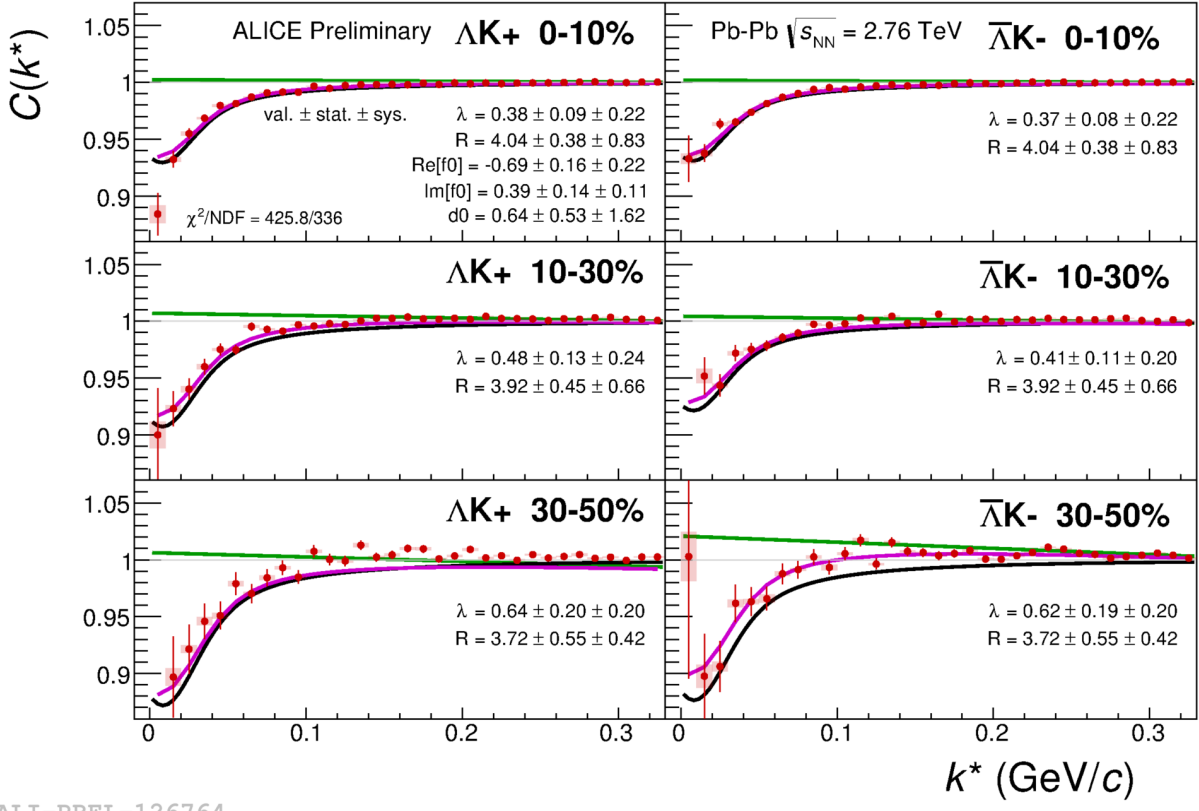


**Fig. 20:** Same as Fig. 19, but with a wider range of view. Fits to the  $\Lambda K_S^0$  (left) and  $\bar{\Lambda} K_S^0$  (right) data for the centralities 0-10% (top), 10-30% (middle), and 30-50% (bottom). The lines represent the statistical errors, while the boxes represent the systematic errors. Each has unique  $\lambda$  and normalization parameters. The radii are shared amongst like centralities; the scattering parameters ( $\mathbb{R} f_0$ ,  $\mathbb{I} f_0$ ,  $d_0$ ) are shared amongst all. The black solid line represents the “raw” fit, i.e. not corrected for momentum resolution effects nor non-flat background. The green line shows the fit to the non-flat background. The purple points show the fit after momentum resolution and non-flat background corrections have been applied. The initial values of the parameters is listed, as well as the final fit values with uncertainties. Here,  $R$  was restricted to [2.,10.] and  $\Lambda$  was restricted to [0.1,0.8].



ALI-PREL-126764

**Fig. 21:** Fits to the  $\Lambda K^+$  (left) and  $\bar{\Lambda} K^-$  (right) data for the centralities 0-10% (top), 10-30% (middle), and 30-50% (bottom). The lines represent the statistical errors, while the boxes represent the systematic errors. Each has unique  $\lambda$  and normalization parameters. The radii are shared amongst like centralities; the scattering parameters ( $\text{Re}[f_0]$ ,  $\text{Im}[f_0]$ ,  $d_0$ ) are shared amongst all. The black solid line represents the “raw” fit, i.e. not corrected for momentum resolution effects nor non-flat background. The green line shows the fit to the non-flat background. The purple points show the fit after momentum resolution and non-flat background corrections have been applied. The initial values of the parameters is listed, as well as the final fit values with uncertainties.

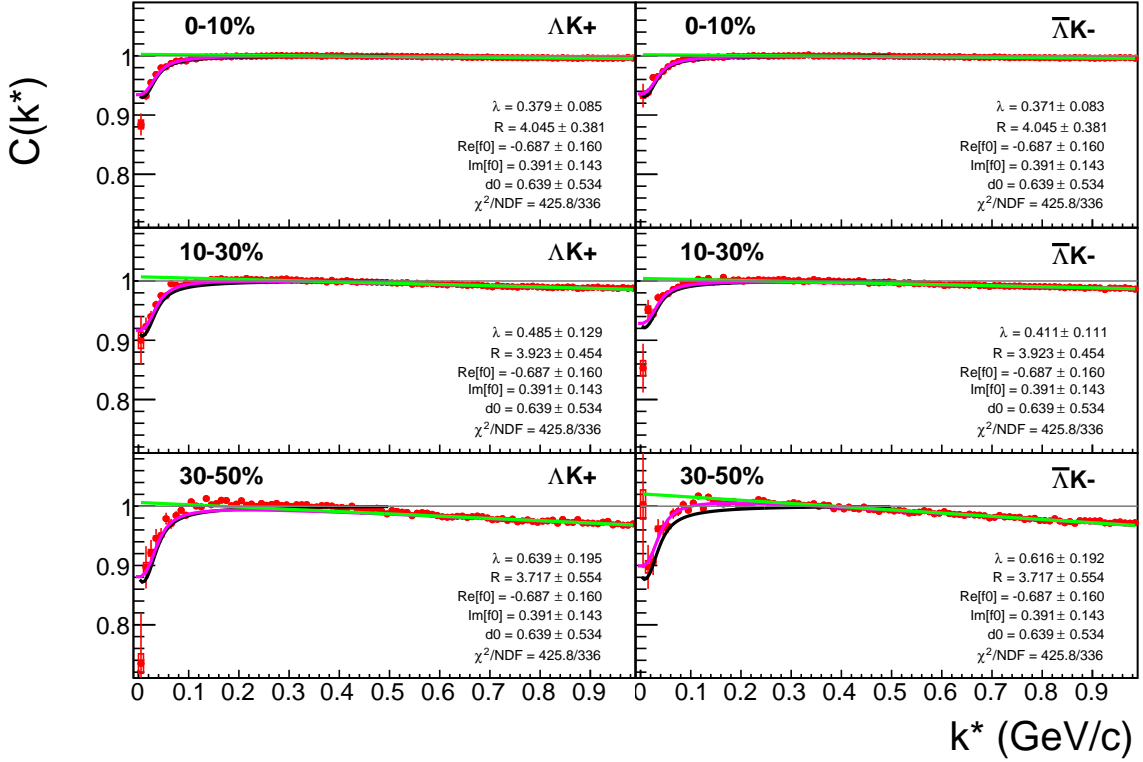


**Fig. 22:** Same as Fig. 21, but with a wider range of view. Fits to the  $\Lambda K^+$  (left) and  $\bar{\Lambda} K^-$  (right) data for the centralities 0-10% (top), 10-30% (middle), and 30-50% (bottom). The lines represent the statistical errors, while the boxes represent the systematic errors. Each has unique  $\lambda$  and normalization parameters. The radii are shared amongst like centralities; the scattering parameters ( $\mathbb{R} f_0$ ,  $\mathbb{I} f_0$ ,  $d_0$ ) are shared amongst all. The black solid line represents the “raw” fit, i.e. not corrected for momentum resolution effects nor non-flat background. The green line shows the fit to the non-flat background. The purple points show the fit after momentum resolution and non-flat background corrections have been applied. The initial values of the parameters is listed, as well as the final fit values with uncertainties.

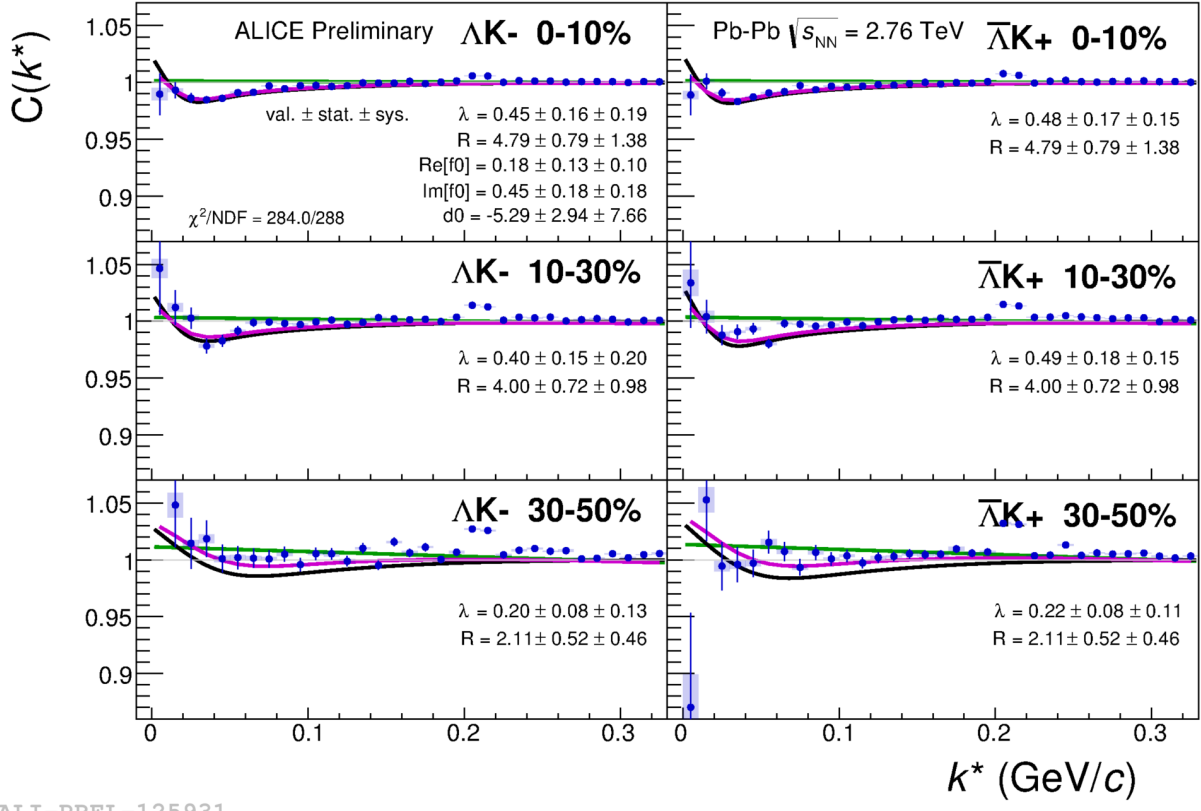


**Fig. 23:** Fits to the  $\Lambda K^-$  (left) with  $\bar{\Lambda} K^+$  (right) data for the centralities 0-10% (top), 10-30% (middle), and 30-50% (bottom). The lines represent the statistical errors, while the boxes represent the systematic errors. Each has unique  $\lambda$  and normalization parameters. The radii are shared amongst like centralities; the scattering parameters ( $Re[f_0]$ ,  $Im[f_0]$ ,  $d_0$ ) are shared amongst all. The black solid line represents the “raw” fit, i.e. not corrected for momentum resolution effects nor non-flat background. The green line shows the fit to the non-flat background. The purple points show the fit after momentum resolution and non-flat background corrections have been applied. The initial values of the parameters is listed, as well as the final fit values with uncertainties.

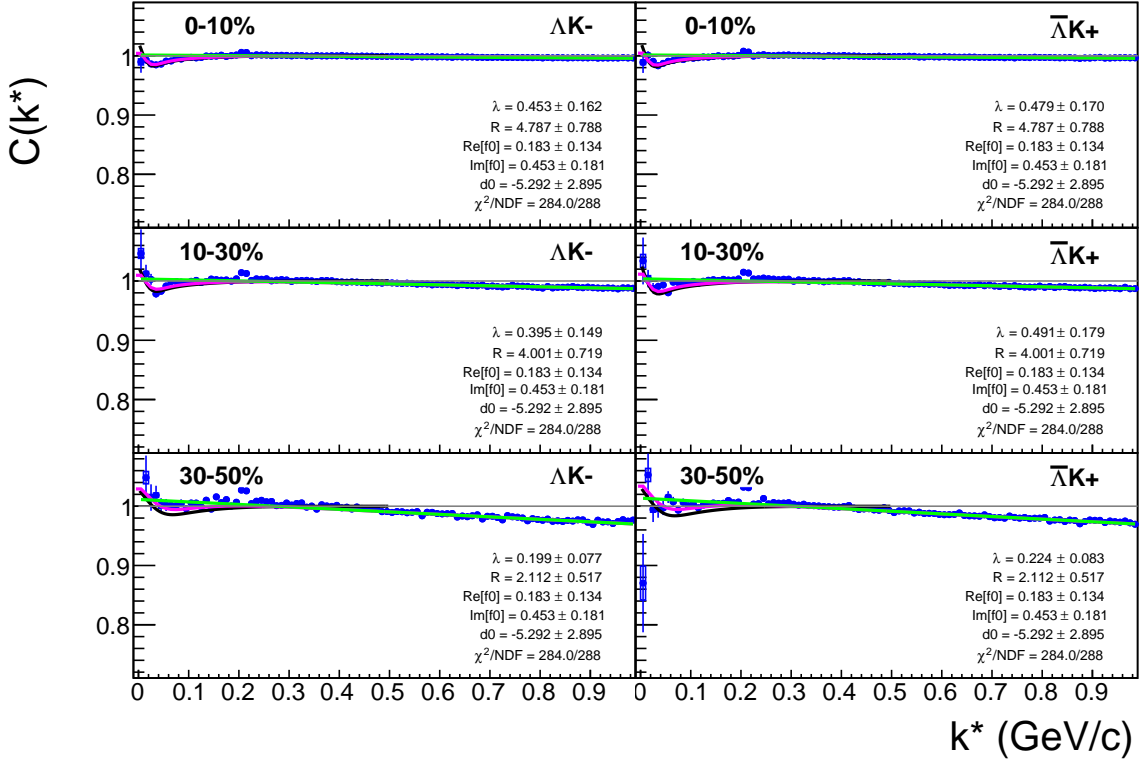


**Fig. 24:** Same as Fig. 23, but with a wider range of view. Fits to the  $\Lambda K^-$  (left) with  $\bar{\Lambda} K^+$  (right) data for the centralities 0-10% (top), 10-30% (middle), and 30-50% (bottom). The lines represent the statistical errors, while the boxes represent the systematic errors. Each has unique  $\lambda$  and normalization parameters. The radii are shared amongst like centralities; the scattering parameters ( $\text{Re}[f_0]$ ,  $\text{Im}[f_0]$ ,  $d_0$ ) are shared amongst all. The black solid line represents the “raw” fit, i.e. not corrected for momentum resolution effects nor non-flat background. The green line shows the fit to the non-flat background. The purple points show the fit after momentum resolution and non-flat background corrections have been applied. The initial values of the parameters is listed, as well as the final fit values with uncertainties.

Fit Results $\Lambda(\bar{\Lambda})K_S^0$						
Pair Type	Centrality	Fit Parameters				
		$\lambda$	$R$	$\mathbb{R}f_0$	$\mathbb{I}f_0$	$d_0$
$\Lambda K_S^0$	0-10%	$0.400 \pm 0.187$ (stat.) $\pm 0.116$ (sys.)	$3.024 \pm 0.541$ (stat.) $\pm 0.329$ (sys.)	$-0.157 \pm 0.031$ (stat.) $\pm 0.043$ (sys.)	$0.176 \pm 0.077$ (stat.) $\pm 0.059$ (sys.)	$3.566 \pm 0.947$ (stat.) $\pm 2.836$ (sys.)
	10-30%		$2.270 \pm 0.413$ (stat.) $\pm 0.324$ (sys.)			
	30-50%		$1.669 \pm 0.307$ (stat.) $\pm 0.280$ (sys.)			
$\bar{\Lambda} K_S^0$	0-10%	$0.400 \pm 0.187$ (stat.) $\pm 0.116$ (sys.)	$3.024 \pm 0.541$ (stat.) $\pm 0.329$ (sys.)	$-0.157 \pm 0.031$ (stat.) $\pm 0.043$ (sys.)	$0.176 \pm 0.077$ (stat.) $\pm 0.059$ (sys.)	$3.566 \pm 0.947$ (stat.) $\pm 2.836$ (sys.)
	10-30%		$2.270 \pm 0.413$ (stat.) $\pm 0.324$ (sys.)			
	30-50%		$1.669 \pm 0.307$ (stat.) $\pm 0.280$ (sys.)			

**Table 1:** Fit Results  $\Lambda(\bar{\Lambda})K_S^0$ . Each pair is fit simultaneously with its conjugate (ie.  $\Lambda K_S^0$  with  $\bar{\Lambda} K_S^0$ ) across all centralities (0-10%, 10-30%, 30-50%), for a total of 6 simultaneous analyses in the fit. Each analysis has a unique  $\lambda$  and normalization parameter. The radii are shared between analyses of like centrality, as these should have similar source sizes. The scattering parameters ( $\mathbb{R}f_0$ ,  $\mathbb{I}f_0$ ,  $d_0$ ) are shared amongst all. The fit is done on the data with only statistical error bars. The errors marked as “stat.” are those returned by MINUIT. The errors marked as “sys.” are those which result from my systematic analysis (as outlined in Section 6).

Fit Results $\Lambda(\bar{\Lambda})K^\pm$						
Pair Type	Centrality	Fit Parameters				
		$\lambda$	$R$	$\mathbb{R}f_0$	$\mathbb{I}f_0$	$d_0$
$\Lambda K^+$	0-10%	$0.379 \pm 0.085$ (stat.) $\pm 0.220$ (sys.)	$4.045 \pm 0.381$ (stat.) $\pm 0.830$ (sys.)	$-0.687 \pm 0.160$ (stat.) $\pm 0.223$ (sys.)	$0.391 \pm 0.143$ (stat.) $\pm 0.111$ (sys.)	$0.639 \pm 0.534$ (stat.) $\pm 1.621$ (sys.)
	10-30%		$0.485 \pm 0.129$ (stat.) $\pm 0.241$ (sys.)	$3.923 \pm 0.454$ (stat.) $\pm 0.663$ (sys.)		
	30-50%		$0.639 \pm 0.195$ (stat.) $\pm 0.204$ (sys.)	$3.717 \pm 0.554$ (stat.) $\pm 0.420$ (sys.)		
$\bar{\Lambda} K^-$	0-10%	$0.371 \pm 0.083$ (stat.) $\pm 0.217$ (sys.)	$4.045 \pm 0.381$ (stat.) $\pm 0.830$ (sys.)			
	10-30%		$0.411 \pm 0.111$ (stat.) $\pm 0.201$ (sys.)	$3.923 \pm 0.454$ (stat.) $\pm 0.663$ (sys.)		
	30-50%		$0.616 \pm 0.192$ (stat.) $\pm 0.203$ (sys.)	$3.717 \pm 0.554$ (stat.) $\pm 0.420$ (sys.)		
$\Lambda K^-$	0-10%	$0.453 \pm 0.162$ (stat.) $\pm 0.186$ (sys.)	$4.787 \pm 0.788$ (stat.) $\pm 1.375$ (sys.)	$0.183 \pm 0.134$ (stat.) $\pm 0.095$ (sys.)	$0.453 \pm 0.181$ (stat.) $\pm 0.184$ (sys.)	$-5.292 \pm 2.895$ (stat.) $\pm 7.658$ (sys.)
	10-30%		$0.395 \pm 0.149$ (stat.) $\pm 0.198$ (sys.)	$4.001 \pm 0.719$ (stat.) $\pm 0.978$ (sys.)		
	30-50%		$0.199 \pm 0.077$ (stat.) $\pm 0.132$ (sys.)	$2.112 \pm 0.517$ (stat.) $\pm 0.457$ (sys.)		
$\bar{\Lambda} K^+$	0-10%	$0.479 \pm 0.170$ (stat.) $\pm 0.152$ (sys.)	$4.787 \pm 0.788$ (stat.) $\pm 1.375$ (sys.)			
	10-30%		$0.491 \pm 0.179$ (stat.) $\pm 0.148$ (sys.)	$4.001 \pm 0.719$ (stat.) $\pm 0.978$ (sys.)		
	30-50%		$0.224 \pm 0.083$ (stat.) $\pm 0.106$ (sys.)	$2.112 \pm 0.517$ (stat.) $\pm 0.457$ (sys.)		

**Table 2:** Fit Results  $\Lambda(\bar{\Lambda})K^\pm$  Each pair is fit simultaneously with its conjugate (ie.  $\Lambda K^+$  with  $\bar{\Lambda} K^-$  and  $\Lambda K^-$  with  $\bar{\Lambda} K^+$ ) across all centralities (0-10%, 10-30%, 30-50%), for a total of 6 simultaneous analyses in the fit. Each analysis has a unique  $\lambda$  and normalization parameter. The radii are shared between analyses of like centrality, as these should have similar source sizes. The scattering parameters ( $\mathbb{R}f_0$ ,  $\mathbb{I}f_0$ ,  $d_0$ ) are shared amongst all. The fit is done on the data with only statistical error bars. The errors marked as “stat.” are those returned by MINUIT. The errors marked as “sys.” are those which result from my systematic analysis (as outlined in Section 6).

**Fit Parameters (value  $\pm$  statistical error  $\pm$  systematic error)**

Pair Type	Centrality	R		
		$\Re f_0$	$\Im f_0$	$d_0$
$\Lambda K^+ & \bar{\Lambda} K^-$	0-10%		<b><math>4.04 \pm 0.38 \pm 0.83</math></b>	
	10-30%		<b><math>3.92 \pm 0.45 \pm 0.66</math></b>	
	30-50%		<b><math>3.72 \pm 0.55 \pm 0.42</math></b>	
		<b><math>-0.69 \pm 0.16 \pm 0.22</math></b>	<b><math>0.39 \pm 0.14 \pm 0.11</math></b>	<b><math>0.64 \pm 0.53 \pm 1.62</math></b>
$\Lambda K^- & \bar{\Lambda} K^+$	0-10%		<b><math>4.79 \pm 0.79 \pm 1.38</math></b>	
	10-30%		<b><math>4.00 \pm 0.72 \pm 0.98</math></b>	
	30-50%		<b><math>2.11 \pm 0.52 \pm 0.46</math></b>	
		<b><math>0.18 \pm 0.13 \pm 0.10</math></b>	<b><math>0.45 \pm 0.18 \pm 0.18</math></b>	<b><math>-5.29 \pm 2.94 \pm 7.66</math></b>
$\Lambda K_S^0 & \bar{\Lambda} K_S^0$	0-10%		<b><math>3.02 \pm 0.54 \pm 0.33</math></b>	
	10-30%		<b><math>2.27 \pm 0.41 \pm 0.32</math></b>	
	30-50%		<b><math>1.67 \pm 0.30 \pm 0.28</math></b>	
		<b><math>-0.16 \pm 0.03 \pm 0.04</math></b>	<b><math>0.18 \pm 0.08 \pm 0.06</math></b>	<b><math>3.57 \pm 0.95 \pm 2.84</math></b>

Figure 25 shows extracted  $R_{\text{inv}}$  parameters as a function of transverse mass ( $m_T$ ) for various pair systems over several centralities. The published ALICE data [6] is shown with transparent, open symbols. The new AK results are shown with opaque, filled symbols. The radii show an increasing size with increasing centrality, as is expected from the simple geometric picture of the collisions. The radii decrease in size with increasing  $m_T$ , and we see an approximate scaling of the radii with transverse mass, as is expected in the presence of collective flow in the system.

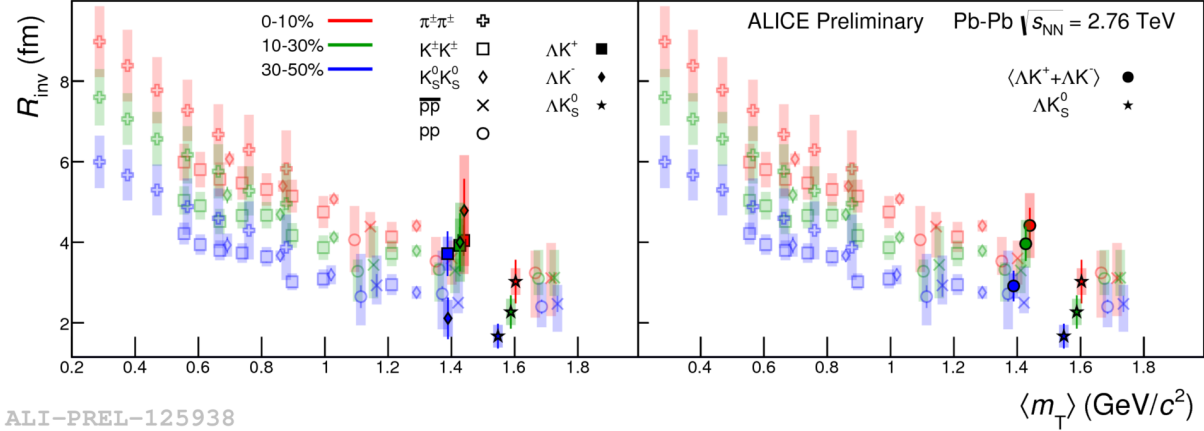


**Fig. 25:** Extracted fit  $R_{\text{inv}}$  parameters as a function of pair transverse mass ( $m_T$ ) for various pair systems over several centralities. The ALICE published data [6] is shown with transparent, open symbols. The new AK results are shown with opaque, filled symbols. In the left, the  $\Lambda K^+$  (with it's conjugate pair) results are shown separately from the  $\Lambda K^-$  (with it's conjugate pair) results. In the right, all  $\Lambda K^\pm$  results are averaged.

## 563 7.2 Results: $\Xi K^\pm$

Even without any fits to the data, the fact that the  $\Xi^- K^+$  data dips below unity (Fig. 26) is exciting, as this cannot occur purely from a Coulomb interaction. We hope that this dip signifies that we are able to peer through the overwhelming contribution from the Coulomb interaction to see the effects arising from the strong interaction.

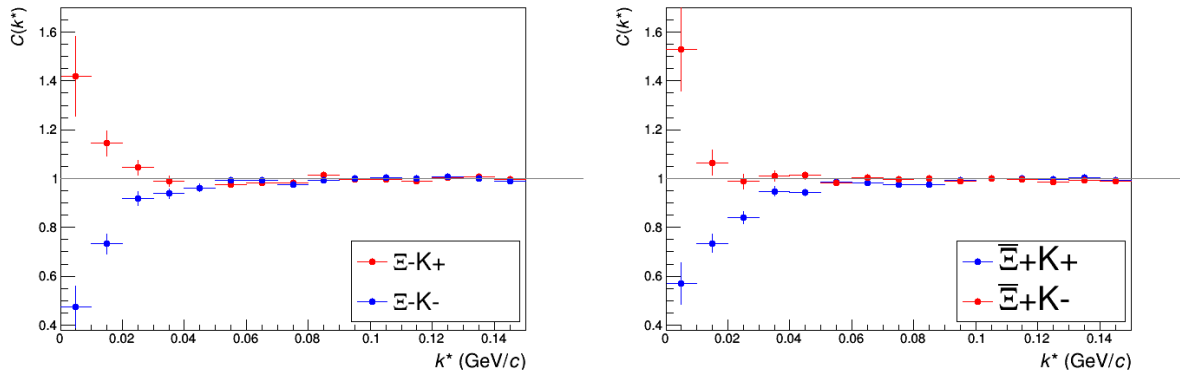


**Fig. 26:**  $\Xi K^\pm$  Results for 0-10% Centrality. (Left)  $\Xi^- K^+$  and  $\Xi^- K^-$  (Right)  $\Xi^+ K^+$  and  $\Xi^+ K^-$

Figure 27 demonstrates graphically, that the  $\Xi^- K^+$  results cannot be described by solely the Coulomb interaction. In this figure, we present the data along with a Coulomb-only band. The Coulomb-only band is spanned by two Coulomb-only curves, whose parameters are given in the figure. The Coulomb-only curves were generated using a technique identical to the generation of the fit function, described in Sec. 5.2, except, of course, with the nuclear scattering parameters all set to zero. The Coulomb-only

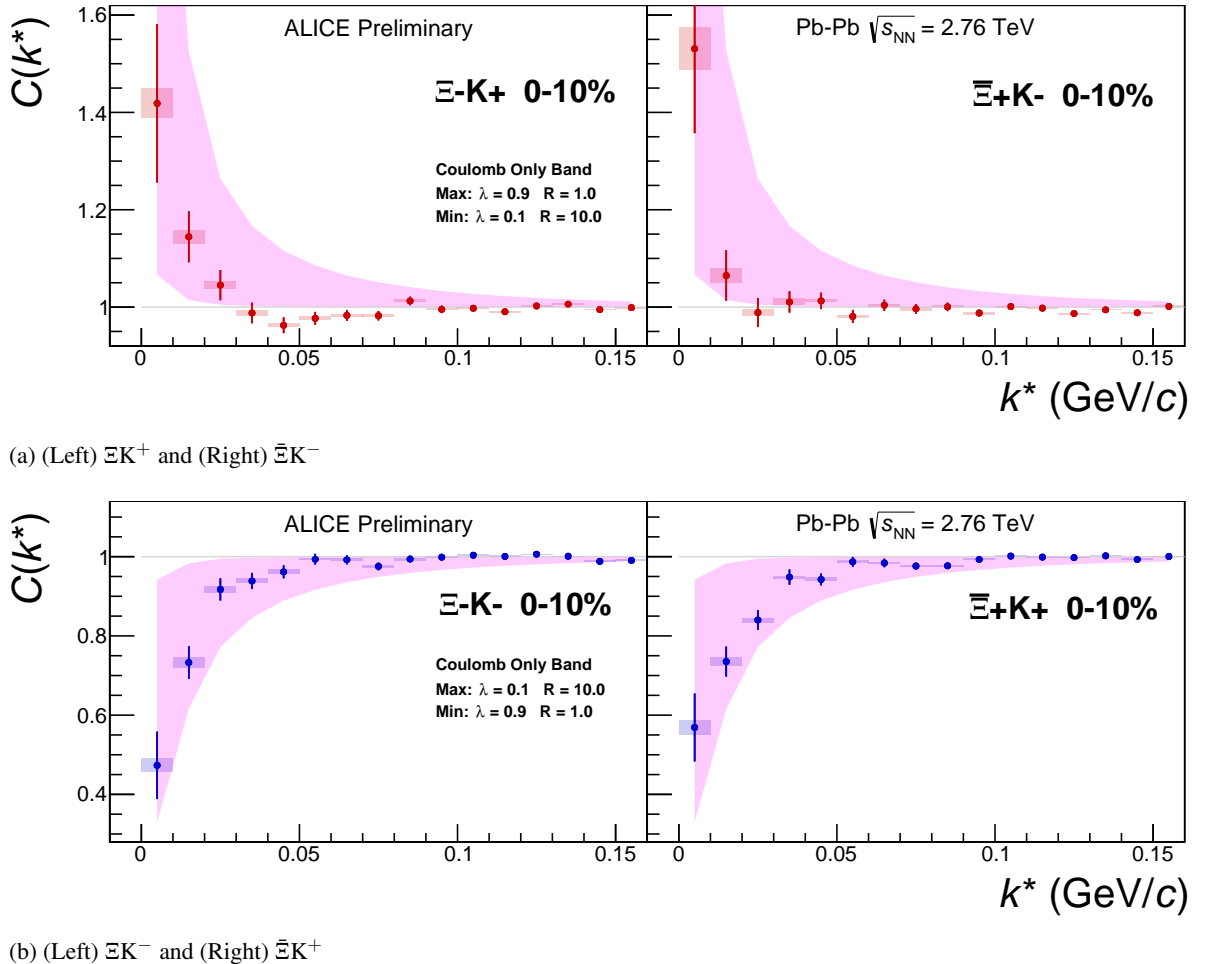


**Fig. 27:**  $\Xi K^\pm$  data with Coulomb-only bands for the 0-10% centrality bin. The Coulomb-only bands span two sets of Coulomb-only curves: (1)  $\lambda = 0.9$ ,  $R = 1.0$  fm and (2)  $\lambda = 0.1$ ,  $R = 10.0$  fm. The Coulomb-only curves are simulated correlation functions for the respective pair system assuming only a Coulomb interaction, i.e. ignoring the strong interaction. The Coulomb-only curves change monotonically with varying  $\lambda$  and varying  $R$ , therefore, any intermediate parameter set will fall within this Coulomb-only band.

573 curves change monotonically with varying  $\lambda$  or varyin radius parametres, therefore, any curves built with  
574 parameter sets intermediate to those use in the Coulomb-only band will be contained in the band.

575 Including the strong interaction into the simulation can dramatically change the resulting correlation  
576 function, as shown in Figure 28. In the figure, the solid line represents a Coulomb-only curve, i.e. a  
577 simulated correlation function with the strong interaction turned off. The dashed lines represent a full  
578 simulation, including both the strong and Coulomb interactions. The two dashed lines differ only in the  
579 real part of the assumed scattering length: positive in Set 1, and negative in Set 2. In the top figure,  
580 for the  $\Xi^- K^+$  simulation, we see that parameter set 2, with a negative real part of the scattering length,  
581 causes the simulated curve to dip below unity, as is seen in the data. If there is a parallel to be drawn  
582 between this analysis and the  $\Lambda K$  analysis, we expect to see similar effects in the  $\Lambda K^+$  system and the  
583  $\Xi^- K^+$  systems. In these systems, we could have an  $s\bar{s}$  annihilation picture. Or, another possible way of  
584 thinking about these systems is in terms of net strangeness. The  $\Lambda K^+$  system has  $S=0$ , while the  $\Lambda K^-$   
585 has  $S=-2$ . The  $\Xi^- K^+$  has  $S=-1$ , while the  $\Xi^- K^-$  has  $S=-3$ .

586 The author was asked to perform a global Coulomb-only fit to the data, to ensure that the system truly  
587 could not be described simply by the Coulomb interaction. In order words, in the fit, the strong force was  
588 turned off, and the  $\Xi^- K^+$ ,  $\bar{\Xi}^+ K^-$ ,  $\Xi^- K^-$ ,  $\bar{\Xi}^+ K^+$  systems all share one sinlge radius parameter, while the

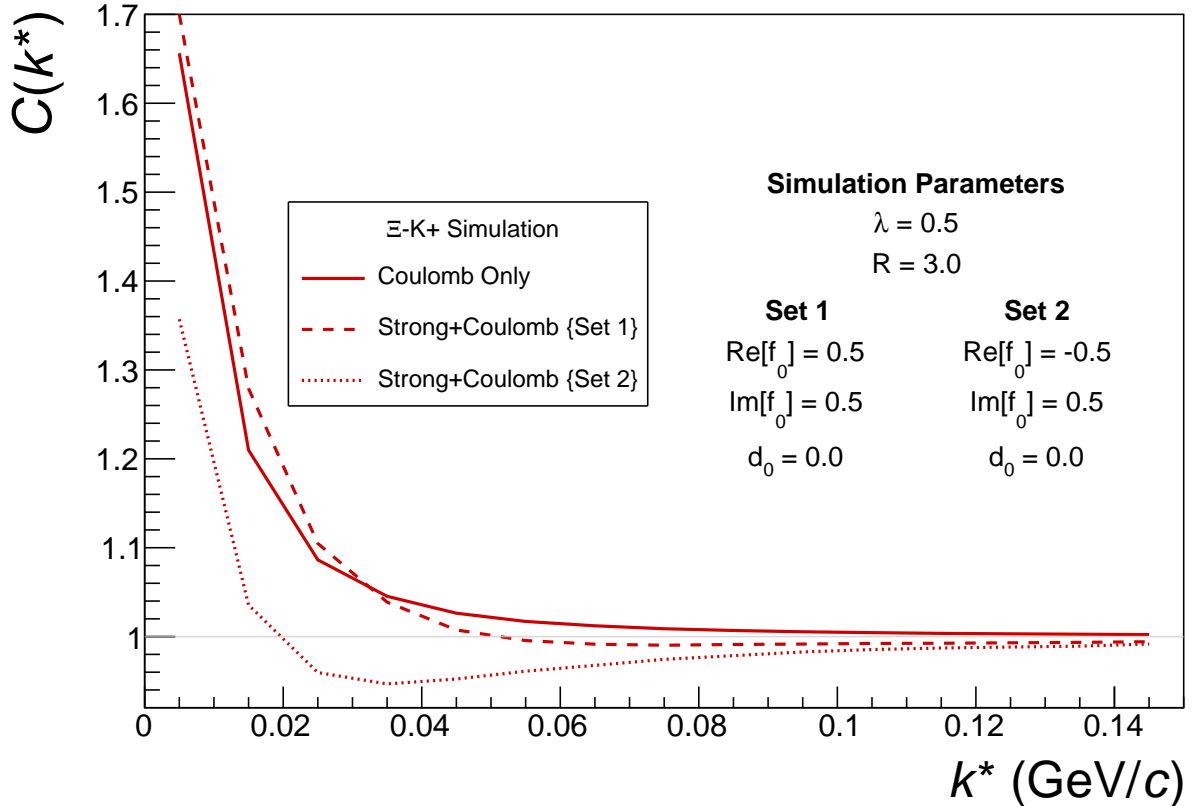
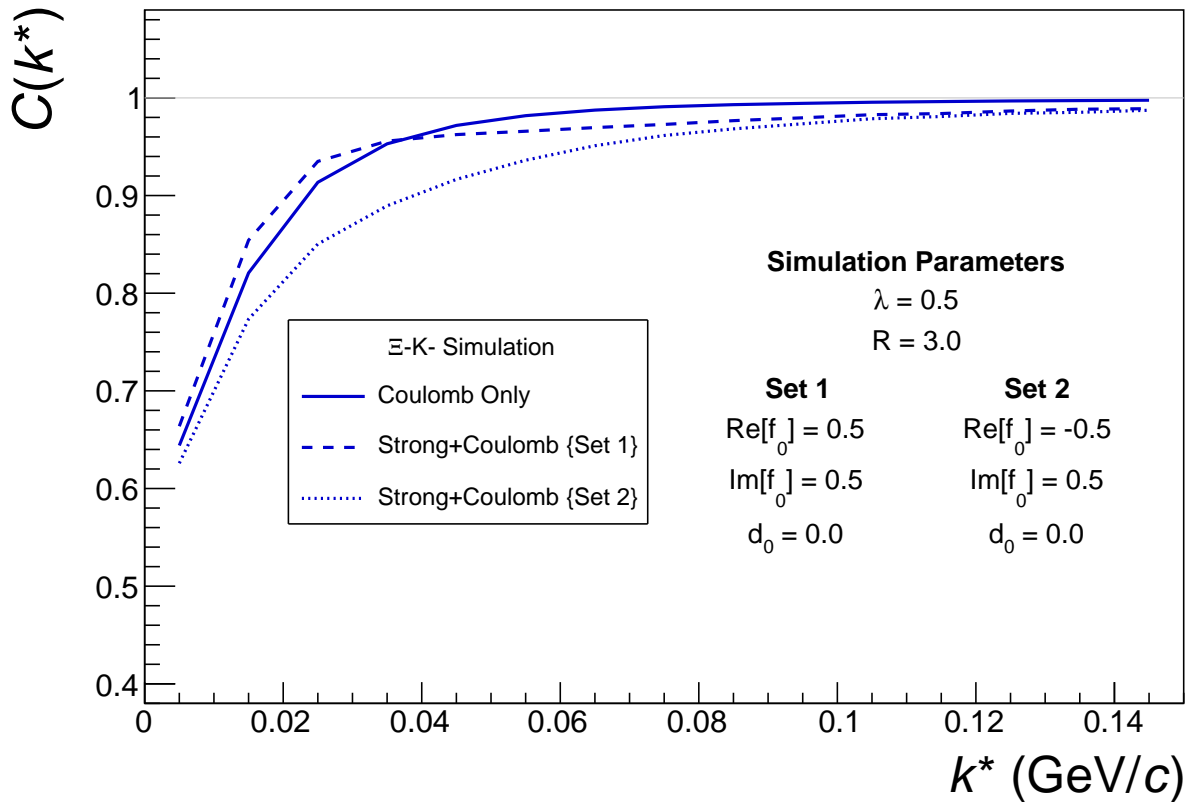
pair and conjugate pair systems share a  $\lambda$  parameter. The results of this fit are shown in Figures 29 and 30. In Fig. 29, there was a lower limit of 0.1 fm placed on the radius parameter, and the radius parameter was initialized to 3 fm (as seems reasonable, when considering the transverse mass of the system and looking at Fig. 25). As is shown in the results, the radius parameter reached this unrealistic lower bound of 0.1 fm. In Fig. 30, the parameters were all unbounded, and the radius parameter was initialized to 10 fm. In this case, the radius parameters reamins high, and ends at an unrealistic value of 10.84 fm. In both cases, the  $\lambda$  parameters are too low. From these figures, we conclude that a global Coulomb-only fit is not suitable for the data.

Although the global Coulomb-only fit failed, it is possible that a Coulomb-only fit performed on  $\Xi^- K^+$  and  $\bar{\Xi}^+ K^-$  separately from  $\Xi^- K^-$  and  $\bar{\Xi}^+ K^+$  could be suitable. The result of such fits are shown in Figures 31 and 32. Figure 31, shows that the fit is not able to describe the dip in the  $\Xi^- K^+$  data below unity. Of course, this is obviously true for an attractive Coulomb-only fit. The radius parameter of 8.43 fm extracted from this fit is unrealistically large. In Figure 32 shows the Coulomb-only fit can described the  $\Xi^- K^-$  data reasonable well; although the extracted radius of 3.73 fm is somewhat larger than expected.

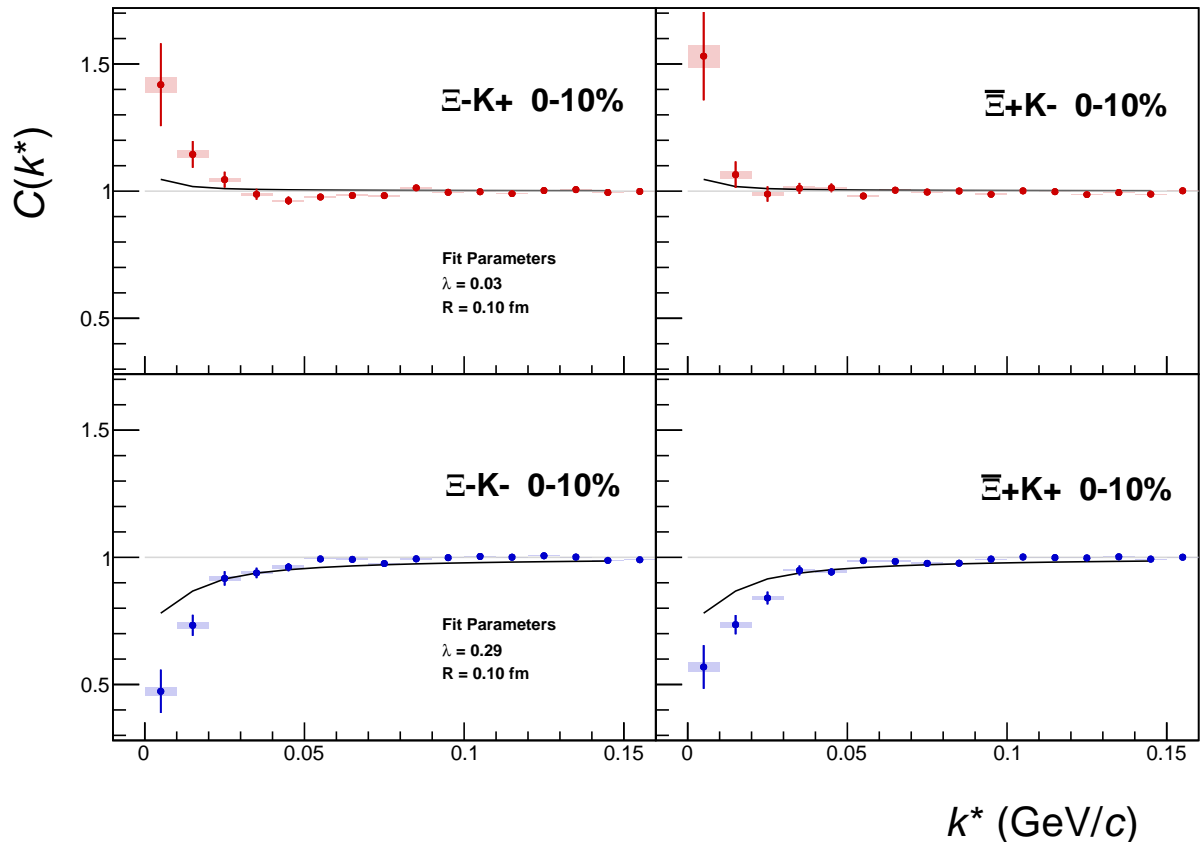
## 8 To Do

### References

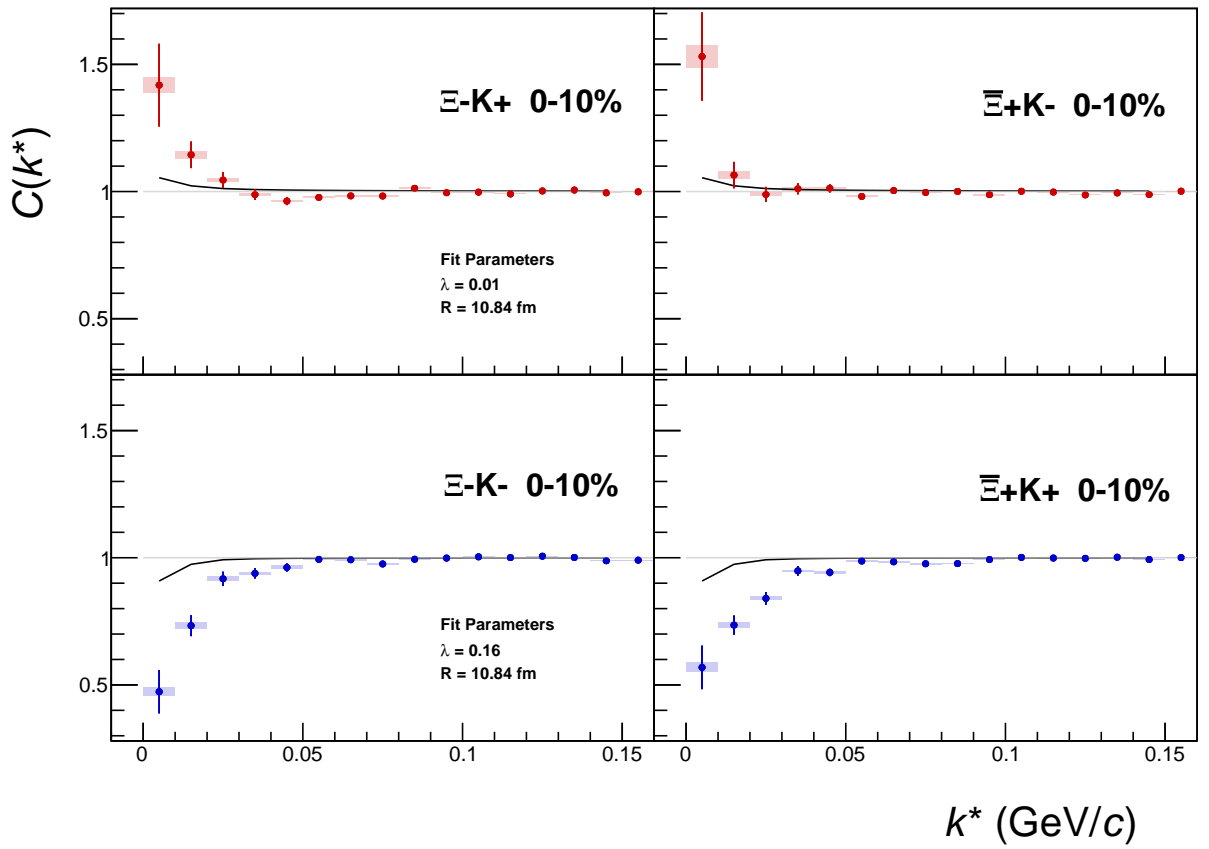
- [1] R. Lednický and V. L. Lyuboshitz. *Sov. J. Nucl. Phys.*, 35:770, 1982.
- [2] Michael Annan Lisa, Scott Pratt, Ron Soltz, and Urs Wiedemann. Femtoscopy in relativistic heavy ion collisions. *Ann. Rev. Nucl. Part. Sci.*, 55:357–402, 2005.
- [3] S. E. Koonin. Proton Pictures of High-Energy Nuclear Collisions. *Phys. Lett.*, B70:43–47, 1977.
- [4] S. Pratt, T. Csorgo, and J. Zimanyi. Detailed predictions for two pion correlations in ultrarelativistic heavy ion collisions. *Phys. Rev.*, C42:2646–2652, 1990.
- [5] Richard Lednický. Finite-size effects on two-particle production in continuous and discrete spectrum. *Phys. Part. Nucl.*, 40:307–352, 2009.
- [6] Jaroslav Adam et al. One-dimensional pion, kaon, and proton femtoscopy in Pb-Pb collisions at  $\sqrt{s_{NN}} = 2.76$  TeV. *Phys. Rev.*, C92(5):054908, 2015.


 (a)  $\Xi K^+$  and  $\bar{\Xi} K^-$  simulation

 (b)  $\Xi K^-$  and  $\bar{\Xi} K^+$  simulation

**Fig. 28:** Effect on the Coulomb-only curve of including the strong interaction for  $\Xi K^\pm$  systems. The solid line represents a Coulomb-only curve, i.e. a simulated correlation function with the strong interaction turned off. The dashed lines represent a full simulation, including both the strong and Coulomb interactions. The two dashed lines differ only in the real part of the assumed scattering length: positive in Set 1, and negative in Set 2.



**Fig. 29:**  $\Xi K^\pm$  Global Coulomb-only fit (Set 1) for 0-10% centrality. In this fit, there was a lower limit of 0.1 fm placed on the radius parameter, and the radius parameter was initialized to 3 fm (as seems reasonable, when considering the transverse mass of the system and looking at Fig. 25). As is shown in the results, the radius parameter reached this unrealistic lower bound of 0.1 fm. Also, the extracted  $\lambda$  parameters are too low.



**Fig. 30:**  $\Xi K^\pm$  Global Coulomb-only fit (Set 2) for 0-10% centrality. In this fit, the parameters were all unbounded, and the radius parameter was initialized to 10 fm. In this case, the radius parameters remain high, and ends at an unrealistic value of 10.84 fm. Also, the extracted  $\lambda$  parameters are too low.

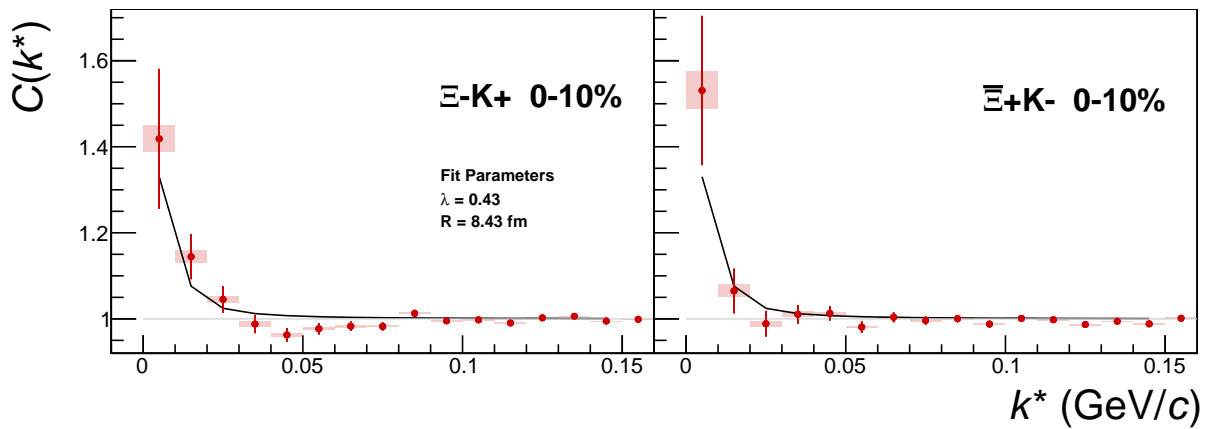


**Fig. 31:**  $\Xi^- K^+$  Coulomb-only fit for 0-10% centrality

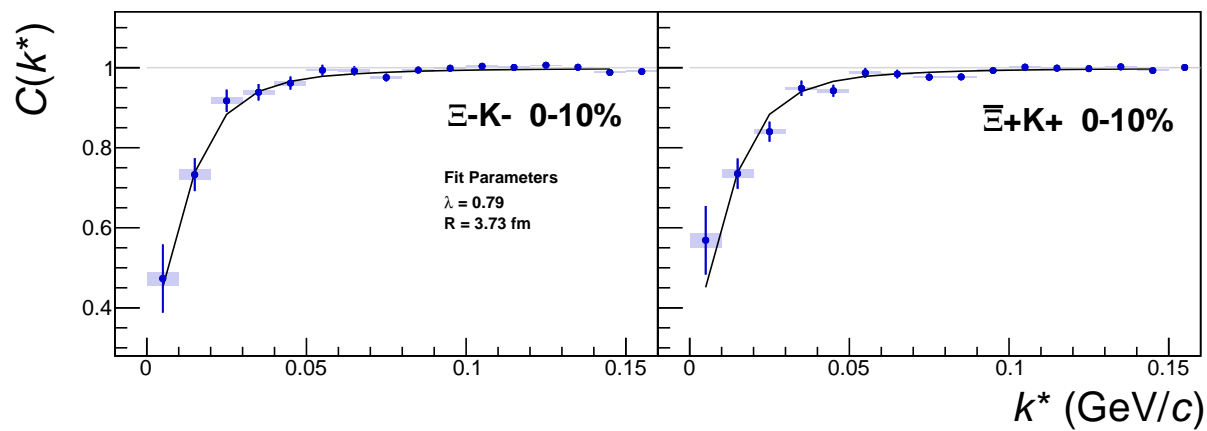


**Fig. 32:**  $\Xi^- K^-$  Coulomb-only fit for 0-10% centrality